Monthly Notices
of the
ROYAL ASTRONOMICAL SOCIETY

MNRAS **444,** 1369–1388 (2014) doi:10.1093/mnras/stu1503

More Kronoseismology with Saturn's rings

M. M. Hedman[1]★ and P. D. Nicholson[2]

[1]*Department of Physics, University of Idaho, Moscow, ID 83844-0903, USA*
[2]*Department of Astronomy, Cornell University, Ithaca, NY 14850, USA*

Accepted 2014 July 24. Received 2014 July 23; in original form 2014 June 10

ABSTRACT

In a previous paper, we developed tools which allowed us to confirm that several of the waves in Saturn's rings were likely generated by resonances with fundamental sectoral normal modes inside Saturn itself. Here we use these same tools to examine eight additional waves that are probably generated by structures inside the planet. One of these waves appears to be generated by a resonance with a fundamental sectoral normal mode with azimuthal harmonic number $m = 10$. If this attribution is correct, then the $m = 10$ mode must have a larger amplitude than the modes with $m = 5$–9, since the latter do not appear to generate strong waves. We also identify five waves with pattern speeds between 807° and 834° d^{-1}. Since these pattern speeds are close to the planet's rotation rate, they probably are due to persistent gravitational anomalies within the planet. These waves are all found in regions of enhanced optical depth known as plateaux, but surprisingly the surface mass densities they yield are comparable to the surface mass densities of the background C-ring. Finally, one wave appears to be a one-armed spiral pattern whose rotation rate suggests it is generated by a resonance with a structure inside Saturn, but the nature of this perturbing structure remains unclear. Strangely, the resonant radius for this wave seems to be drifting inwards at an average rate of 0.8 km yr^{-1} over the last 30 yr, implying that the relevant planetary oscillation frequency has been steadily increasing.

Key words: asteroseismology – occultations – planets and satellites: general – planets and satellites: individual: Saturn – planets and satellites: interiors – planets and satellites: rings.

1 INTRODUCTION

Saturn's rings exist in a complex dynamical environment, with various forces perturbing the ring-particles' orbits and forming a multitude of patterns and structures. While the gravitational tugs from Saturn's various moons have long been known to sculpt the rings, asymmetries in the planet's own gravitational field can also produce distinctive patterns in the inner part of the ring system. In particular, Hedman & Nicholson (2013) provided evidence that several spiral density waves in Saturn's C-ring observed in *Voyager* and *Cassini* occultation data (Rosen et al. 1991; Colwell et al. 2009; Baillié et al. 2011) have the right pattern speeds and symmetry properties to be generated by low-order normal mode oscillations within Saturn, as predicted by Marley (1990) and Marley & Porco (1993). Analyses of these patterns yielded precise estimates of the rotation periods of these modes, which should provide novel insights into the planet's deep interior. However, these measurements also revealed that there were multiple patterns with the same basic symmetry but slightly different pattern speeds. Such fine splitting of the normal modes was not predicted and might suggest that current models of Saturn's internal structure are incomplete (Fuller, Lai & Storch 2014; Marley 2014).

The analysis performed by Hedman & Nicholson (2013) focused on six density waves which had the strongest opacity variations and the longest wavelengths. These waves were the easiest ones to study and measure, and indeed we obtained extremely precise and robust estimates of these patterns' rotation rates around the planet. However, many more wave-like patterns exist in the C-ring (Baillié et al. 2011), and these same techniques could potentially be applied to these features. In this work, we estimate the pattern speeds and symmetry properties of several additional waves that provide further information about the planet's internal structure.

Section 2 provides a brief summary of our methods for analysing unidentified density waves in occultation data, while Section 3 lists the known C-ring waves that could be investigated with these techniques. Section 4 focuses on a wave that appears to provide another example of a feature generated by a resonance with a low-order normal mode oscillation within the planet. This feature raises interesting questions about the amplitude spectra of these normal modes. Another, weaker wave in the same region that may be generated by a planetary normal mode is considered in Section 5. Unfortunately, the signal-to-noise ratio of this feature turns out to be too low to yield a definitive identification at this time. Section 6 considers several patterns that do not appear to be driven by normal mode

★ E-mail: mhedman@uidaho.edu

oscillations, but instead could be caused by gravitational anomalies moving around the planet at close to Saturn's rotation rate. Besides providing new information about the planet's internal structure, these waves reveal surprising trends in the C-ring's surface mass density. Section 7 describes a curious wave that appears to be propagating in the wrong direction given its pattern speed, and has been moving slowly through the rings over the last 30 yr. Finally, we summarize the conclusions of this investigation.

2 METHODS

As in Hedman & Nicholson (2013), we use wavelet-based techniques in order to ascertain the symmetry properties and pattern speeds of various density-wave patterns observed in multiple occultation profiles obtained by the Visual and Infrared Mapping Spectrometer (VIMS) onboard the *Cassini* spacecraft. For the sake of completeness, we will provide a summary of our analysis methods, and refer the reader to Hedman & Nicholson (2013) for more details on these techniques.

During an occultation, VIMS measures the apparent brightness of a star as a function of time while the star passes behind the rings. Since VIMS has a highly linear response curve (Brown et al. 2004), these measurements of the star's brightness can be readily transformed into estimates of the ring's opacity at the location where the starlight passes through the rings. This opacity can be expressed in terms of the transmission T, the optical depth along the line of sight $\tau = -\ln(T)$ or the normal optical depth $\tau_n = \tau \sin|B|$ (where B is the angle between the line of sight to the star and the ring plane). The location where the light passed through the ring during each measurement is estimated using a combination of the precise time stamps associated with the occultation data, the reconstructed trajectory of the spacecraft (from the NAIF website)[1] and the location of the star on the sky (derived from the *Hipparcos* catalogue,[2] and corrected for proper motion and parallax at Saturn). Each occultation therefore yields a profile of the ring's opacity as a function of ring radius, longitude and time. Based on the positions of sharp ring edges in these profiles, we find that our reconstruction of the occultation geometry is accurate to within several hundred metres. Furthermore, a global analysis of all the occultation data by R. French provides slight trajectory corrections. These corrections yield radial position estimates that are good to within 200 m, which is more than sufficient for the purposes of this analysis.

Within each profile, density waves appear as quasi-periodic variations in the ring's opacity with wavelengths that systematically vary with radius (see Figs 3, 8 and 15). However, the positions of individual peaks and troughs vary from occultation to occultation because the entire wave is actually a tightly wound spiral pattern, and different occultations cut through this pattern at different locations and times. Two parameters characterize these azimuthal variations: an integer m that determines the number of arms in the spiral pattern, and the speed at which the entire pattern rotates around the planet. If the spiral pattern is generated by a first-order Lindblad resonance, then this pattern speed Ω_p is given by the following expression:

$$\Omega_p = \frac{(m-1)n + \dot{\varpi}}{m}, \tag{1}$$

where n is the local orbital mean motion, and $\dot{\varpi}$ is the local apsidal precession rate. Note that Ω_p can be slower or faster than n, depending on whether m is positive or negative. Waves with $m > 0$ and $\Omega_p < n$ are associated with inner Lindblad resonances and are expected to propagate outwards, while those with $m < 0$ and $\Omega_p > n$ are associated with outer Lindblad resonances and should propagate inwards. Both types of patterns have $|m|$ arms, so the azimuthal location of a given cut through the pattern can be quantified in terms of a phase parameter:

$$\phi = |m|(\lambda - \Omega_p t), \tag{2}$$

where λ and t are the inertial longitude and time of the occultation. So long as the amplitude of the wave is small, the optical depth variations associated with the wave can be written as

$$\tau(r) \simeq \tau_0 + \Delta\tau(r)\cos(\phi + \phi_r(r)), \tag{3}$$

where $\Delta\tau(r)$ is a slowly varying amplitude and $\phi_r(r)$ is a monotonically increasing function of r that determines the local radial wavelength of the pattern. One can therefore regard ϕ as a measure of where the peaks and troughs of the profile are found in a given profile obtained at a particular longitude and time. (If we choose a suitable radius r_0 in the wave where $\phi_r = 0$, then $\phi = 0$ corresponds to a profile where there is an opacity maximum at r_0, while $\phi = 180^\circ$ corresponds to a profile with a minimum in opacity at the same r_0.)

In practice, accurately measuring the absolute value of the phase ϕ for an unidentified wave is challenging because the radial wavelength of the wave varies smoothly with radius (i.e. $d\phi_r/dr$ is not a constant), so the phase estimate at a particular radius for a given occultation profile is sensitive to how well these trends can be modelled. By contrast, the phase difference between two profiles $\delta\phi$ is easier to determine because this difference should be a constant across the entire wave. We therefore compute $\delta\phi$ for each pair of occultations using wavelet transforms. Again, we will simply outline our procedures here, and refer the interested reader to Hedman & Nicholson (2013) for the relevant details. First, we interpolate the data from each occultation on to a regular array of radii and compute a wavelet transform using the standard IDL routine WAVELET (Torrence & Compo 1998). Next, we compute the wavelet power and weighted average wavelet phase $\phi + \phi_r$ for each profile as a function of radius in a specified spatial wavelength band. In Hedman & Nicholson (2013) the wavelength range used was from 0.1 to 5 km, but here we will use different ranges for different waves. Next, we compute $\delta\phi$ between two cuts as the weighted average difference of the two phase profiles, using the average power in the two profiles as the weighting function.

As before, we visually inspect the occultation profiles and only consider observations where the wave is clearly resolved and data gaps do not corrupt multiple wave cycles. We also automatically exclude $\delta\phi$ estimates from any pair of occultations where the average of the two power profiles is never more than 0.9 times the normalized peak signal in either individual profile (which indicates the peak signal is being measured in disjoint regions) or if the standard deviation of the phase differences to be averaged together exceeds 20° (which indicates the phase difference is not being accurately measured). Depending on the analysis, we also exclude pairs with time separations longer than either 300 or 1000 d, simply to reduce the effects of aliasing.

For any given trial values of m and pattern speed Ω_p, we can compute the expected phase difference between each pair of profiles:

$$\delta\phi_{pred} = |m|(\delta\lambda - \Omega_p \delta t), \tag{4}$$

where $\delta\lambda$ and δt are the difference in the observed inertial longitudes and observation times for the two occultations. We then compare these predicted values to the observed values of $\delta\phi$ to

[1] http://naif.jpl.nasa.gov/pub/naif/CASSINI/

[2] http://hesarc.gsfc.nasa.gov/W3Browse/hipparcos.html. Perryman et al. (1997).

Table 1. Summary of wave-like C-ring features.

Baillié et al. feature	Location	Identification	Comment
1	74 666 km		Not examined, too few VIMS occs with sufficient resolution
2	74 892 km	Mimas 4:1 ILR	See footnote 3
3	74 923 km		Not examined, too few VIMS occs with sufficient resolution
4	74 939 km	Rosen wave-b	Not examined, too few VIMS occs with sufficient resolution
5	76 022 km		Not examined, too few VIMS occs with sufficient resolution
6	76 234 km		Not examined, too few VIMS occs with sufficient resolution
9	76 435 km		Not examined, too few VIMS occs with sufficient resolution
10	76 539 km		Not examined, too few VIMS occs with sufficient resolution
11	76 729 km		Not examined, too few VIMS occs with sufficient resolution
12	77 511 km	Titan −1:0 IVR	See Nicholson et al. (in preparation)
13	80 988 km	W80.98 $m = -4$ pattern	Examined in Hedman & Nicholson (2013)
14	81 018 km	W81.02 ($m = -11? -5?$)	Examined in Section 5
15	82 010 km	W82.01 $m = -3$ pattern	Examined in Hedman & Nicholson (2013)
16	82 061 km	W82.06 $m = -3$ pattern	Examined in Hedman & Nicholson (2013)
17	82 209 km	W82.21 $m = -3$ pattern	Examined in Hedman & Nicholson (2013)
18	83 633 km	W83.63 $m = -10$ pattern	Examined in Section 4
19	84 644 km	W84.64 $m = -2$ pattern	Examined in Hedman & Nicholson (2013)
20	84 814 km	W84.82 $m = +3$ pattern	Examined in Section 6
21	84 857 km	W84.86 $m = +3$ pattern	Examined in Section 6
22	85 105 km	Pan 2:1 ILR	Not examined here, too low signal-to-noise ratio
23	85 450 km	Rosen wave j	Not examined here, too low signal-to-noise ratio
24	85 473 km		Not examined here, too low signal-to-noise ratio
25	85 514 km		Not examined here, too low signal-to-noise ratio
26	85 523 km		Not examined here, too low signal-to-noise ratio
27	85 677 km	W85.67 $m = -1$ pattern	Examined in Section 7
28	86 400 km	W86.40 $m = +3$ pattern	Examined in Section 6
29	86 576 km	W86.58 $m = +3$ pattern	Examined in Section 6
31	86 590 km	W86.59 $m = +3$ pattern	Examined in Section 6
32	87 189 km	W87.19 $m = -2$ pattern	Examined in Hedman & Nicholson (2013)
33	87 647 km	Atlas 2:1 ILR	Not examined here, too low signal-to-noise ratio
34	88 713 km	Prometheus 2:1 ILR	Not examined here, on a complex ringlet
35	88 736 km	$m = +1$	See footnote 4
36	89 883 km	Mimas 6:2 ILR	Examined in Section 6
37	89 894 km	Pandora 4:2 ILR	Examined in Section 6
38	90 156 km	Pandora 2:1 ILR (?)	Not examined here, on complex ringlet
39	90 198 km	Mimas 3:1 ILR	Not examined here, on complex ringlet
40	90 279 km		Not examined, too low signal-to-noise ratio

ascertain which m and Ω_p are most consistent with the observations. In practice, we examine the rms dispersion of the 'phase difference residuals' (i.e. the observed values of $\delta\phi$ minus the predicted values). For most of the waves considered here, we find that for one particular value of m, there is a pronounced minimum in the rms residuals near the predicted pattern speed. This minimum thus provides a fairly unique identification of the symmetry properties and pattern speed of the relevant wave.

3 SELECTING FEATURES TO EXAMINE

We can only extract sensible phase estimates if the occultation profiles have sufficient resolution and signal-to-noise ratio, so we cannot use the techniques described above if the wave's wavelength or amplitude is too small. We therefore conducted a survey of the roughly 40 wave-like features in the C-ring identified by Baillié et al. (2011) in order to ascertain which patterns would be the best ones to investigate. Table 1 summarizes the results of this survey.

There are several sets of waves we are unable to analyse using the currently available VIMS data and the routines described above. More specifically, the features interior to 77 000 km all have rather short wavelengths and we do not have enough VIMS occultations with sufficient resolution to determine the relevant phase differences.[3] Investigations of these structures will therefore likely require higher resolution (<200 m) data from the Ultraviolet Imaging Spectrograph (UVIS) and Radio Science Subsystem (RSS) experiments. We chose not to analyse any of the five waves Baillié et al. (2011) found between 85 000 and 85 500 km, the Atlas 2:1 wave at 87 647 km or the wave at 90 279 km because these features are very weak and could not be clearly discerned in individual VIMS occultation profiles. [Indeed, Baillié et al. (2011) were only able to detect some of these weaker waves by co-adding data from multiple occultations.] Finally, we have elected not to consider the Titan −1:0 bending wave at 77 520 km, or any of the wave-like patterns found within or close to the C-ring's various dense ringlets. These structures are in complex dynamical environments that will likely require modified processing algorithms that we plan to develop in a future work.[4]

[3] We did have sufficient VIMS occultations to confirm that the wave near the Mimas 4:1 inner Lindblad resonance was an $m = 2$ pattern with the correct pattern speed for this resonance.

[4] We did find one wave-like structure at 88 736 km (designated feature 35 by Baillié et al. 2011), which could be analysed using the tools described above. The phase differences derived from that wave indicate that it is an $m = +1$ spiral pattern rotating around the planet at around 14° d^{-1}. This pattern

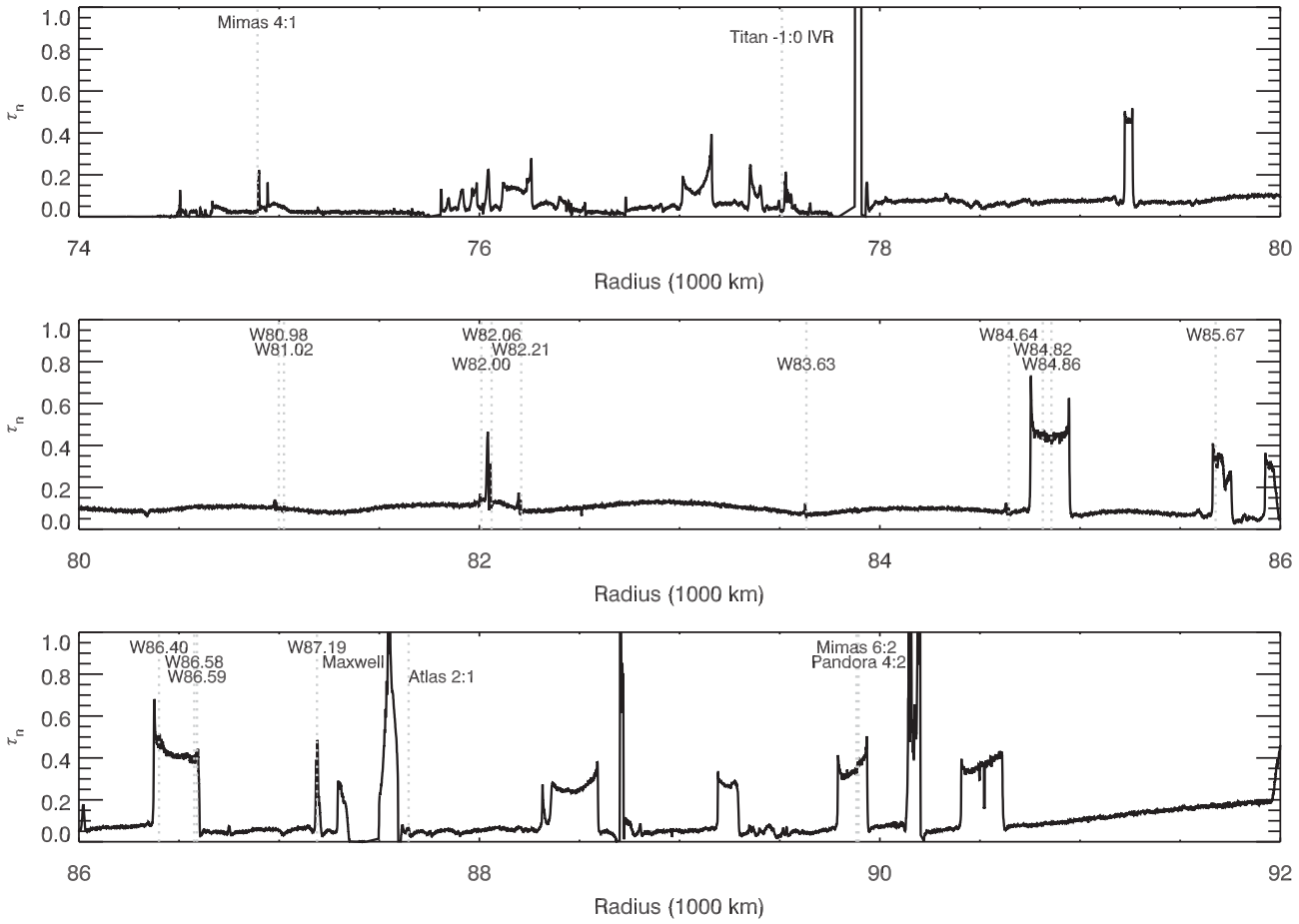

Figure 1. Optical depth profile of the C-ring, derived from the γ Crucis occultation obtained during *Cassini* orbit ('Rev') 89. The profile has been downsampled for display purposes, and the locations of the various waves discussed in the text are marked.

In the end, we found 16 waves that we could productively investigate at this time. The locations of all these features are marked in Fig. 1, while Table 1 and Fig. 2 summarize our conclusions regarding the pattern speeds and symmetry properties for many of these waves. Our analyses indicate that these features can be divided into three broad classes. First, we have the waves that appear to be generated by sectoral normal modes inside the planet. These include the six waves examined in our previous paper, along with two features at 81 018 and 83 633 km that are in the same general part of the rings. Second, we have seven fairly weak waves within features known as 'plateaux' in the outer part of the C-ring. Two of these features were already identified with the 6:2 Mimas and 4:2 Pandora resonances (Baillié et al. 2011), while the other five (found inside plateaux P5 and P7) appear to be $m = +3$ patterns with pattern speeds close to the planet's rotation rate. Finally, there is a very unusual wave in plateau P6 around 85 670 km which actually appears to have moved steadily inwards over the last 30 yr.

Tables 2 and 3 provide lists of the VIMS occultations that were considered in the analysis of each of these waves. Lists of phase difference estimates derived from these profiles are available in an online data supplement, a sample of which is shown in Table 4. For a summary of the results of this investigation, including the inferred m-numbers and pattern speeds of the relevant waves, see Table 5. Note that this analysis includes several occultations that were not part of our earlier study. Re-analysing the original six waves with this larger data set yielded essentially the same results as our previous analysis (compare the relevant entries in Table 5 with table 4 of Hedman & Nicholson 2013).

speed is much slower any predicted resonance with Saturn and instead may indicate some connection with the adjacent Bond ringlet. We will therefore postpone a detailed investigation of this feature to a paper focusing on the waves associated with dense ringlets.

4 W83.63: AN $m = -10$ WAVE

The first wave we will consider here is the one designated W83.63 in Colwell et al. (2009) [it is also called *h* in Rosen et al. (1991) and wave 18 in Baillié et al. (2011)]. An example profile of this wave is shown in Fig. 3, where it is compared with two nearby waves examined by Hedman & Nicholson (2013). Note this wave is found in a low optical-depth region between three waves (W82.00, W82.06 and W82.21) that Hedman & Nicholson (2013) identified as $m = -3$ and another wave (W84.64) that appears to have $m = -2$ (see Fig. 1). As shown in Fig. 3, W83.63 has a much shorter wavelength than either the $m = -3$ or the $m = -2$ waves. W83.63's shorter wavelength means that some of the profiles that could provide useful data on the other waves do not have sufficient resolution to yield sensible phase information for this wave. Furthermore, its shorter wavelength will also make the phase measurements more sensitive to slight geometry errors. Hence we elected not to look at this wave

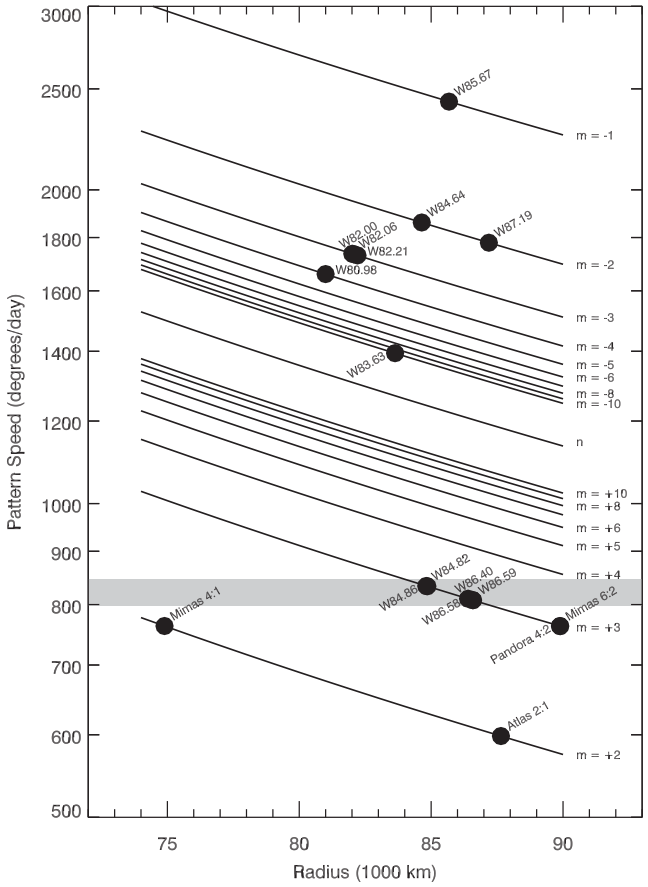

Figure 2. The locations and pattern speeds of various waves in Saturn's C-ring. This plot shows the radius (distance from Saturn centre) and pattern speeds for many of the waves identified by Baillié et al. (2011), Hedman & Nicholson (2013) and this work (no data point is given for wave W81.02 because the identification of this wave is still uncertain). The series of diagonal lines correspond to the expected pattern speeds for first-order Lindblad resonances with different values of m. The lines with negative m values correspond to outer Lindblad resonances, while the lines with positive m values correspond to inner Lindblad resonances. The line marked as n is where the pattern speed would equal the local orbital rate. The grey shaded band corresponds to the range of rotation rates observed in Saturn's visible winds and magnetospheric radio emissions (see Fig. 13).

in our initial study. However, subsequent investigations revealed 19 VIMS occultations with sufficient resolution to yield useful phase data for this wave (see Table 2), and trajectory refinements provided by R. French were sufficiently precise to yield a sensible solution for m and Ω_p. Note that when we computed phase differences between the wave profiles, we considered wavelengths between 0.1 and 5 km.

Since the wave appears to propagate inwards, like the waves described in Hedman & Nicholson (2013), we expected that this wave would have a negative value for m. Indeed, when we examined a range of different m-values, we found the smallest dispersion in the phase residuals occurred with $m = -10$ and a pattern speed close to the expected value for an $m = -10$ wave with a resonant radius $r_L = 83\,633$ km (the estimated resonant radius from Baillié et al. 2011). A profile of the rms residuals as a function of pattern speed (assuming $m = -10$) is provided in Fig. 4, which shows that the best-fitting solution corresponds to $\Omega_p = 1394.^\circ05\ d^{-1}$. This solution has an rms residual of around 45°, roughly two times larger than the scatter around the best-fitting solutions for the better resolved waves examined in Hedman & Nicholson (2013). Nevertheless, the residuals (also shown in Fig. 4) exhibit a reasonably tight distribution around zero with no obvious trends out to 300 d.

Additional, weaker minima can be observed in the rms residuals in the upper panel of Fig. 4. Also, if we assume $m = -9$, we found a single minimum where the rms reaches about 60° for a value of $\Omega_p \sim 0.2^\circ\ d^{-1}$ away from the expected pattern speed. All of these other solutions are substantially worse than the $m = -10$, $\Omega_p = 1394.^\circ05\ d^{-1}$ solution, and so we do not regard them as valid alternatives. Instead, they are likely due to aliasing among the relatively sparse observations. We have also confirmed that $m = -10$, $\Omega_p = 1394.^\circ05\ d^{-1}$ remains the best solution even if we add other observations with somewhat poorer resolution and/or data gaps. Thus we are fairly confident that W83.63 is indeed an $m = -10$ wave.

We may also note that a value of $m = -10$ is plausible based on a consideration of the rings' local surface mass density. The wavelength of a given density wave depends on both the m-value and the (unperturbed) ring surface mass density σ_0, and Baillié et al. (2011) provide scaled estimates of the surface mass density $\sigma_0 = 0.45|m - 1|$ g cm^{-2} and the opacity $\tau_n/\sigma_0 = 0.22/|m - 1|$ cm^2 g^{-1} based on their observations of this wave. If we insert $m = -10$ into these expressions, then we obtain a surface mass density of 4.95 g cm^{-2} and an opacity of 0.020 cm^2 g^{-1} for this wave. These numbers are comparable to the values obtained from the nearby $m = -2$, -3 and -4 waves (see Table 5 and Fig. 14).

The derived value for m is also reasonably consistent with the theoretical predictions by Marley & Porco (1993). While those authors only predicted resonance locations for patterns with $|m|$ between 2 and 8, one can extrapolate from these data to estimate that the resonance with $|m| = 10$ should indeed fall somewhere in the vicinity of W83.63. Combined with the reasonable surface mass density estimate, and the close match between the observed and expected pattern speeds, this makes the identification of W83.63 as an $m = -10$ wave reasonably secure.

The existence of this clear $m = -10$ wave raises some interesting questions about the relative amplitudes of the waves generated by normal modes inside the planet. According to Marley & Porco (1993), each fundamental sectoral (i.e. $\ell = m$) normal mode within the planet gives rise to a wave in the rings with the same azimuthal wavenumber $|m|$, and the amplitude of the wave should depend upon the magnitude of the corresponding planetary normal mode. Hedman & Nicholson (2013) found $m = -2$, -3 and -4 waves with substantial amplitudes in the middle C-ring, which correspond to $m = 2, 3$ and 4 fundamental normal modes within the planet. Now we have another wave with a large amplitude ($\delta\tau/\tau \simeq 1$) that appears to be generated by the $m = 10$ fundamental sectoral normal mode. However, resonances with the $m = 5$ through 9 normal modes should also fall between 80 000 and 84 000 km, and there are no other waves with amplitudes comparable to W83.63 in this region. This is especially surprising because this entire region is largely featureless outside of the relevant waves (see Fig. 1), so it is unlikely that these waves would be lost or obscured by other structures. While further analysis could potentially reveal weak waves within this region, the available data suggest that the $m = 5$–9 planetary normal modes have significantly lower amplitudes than the $m = 10$ mode. This is inconsistent with the expected spectrum of normal modes computed by Marley & Porco (1993, fig. 6) assuming simple mode-energy partition schemes (Goldreich & Kumar 1988, 1990), and implies that the excitation spectrum of the planetary normal modes has a non-trivial shape.

Table 2. Observed times (in seconds of ephemeris time, measured from the J2000 epoch) and inertial longitudes (measured relative to the longitude of ascending node on the J2000 equator) for the occultation cuts through the various waves associated with the outer Lindblad resonances. Blank entries indicate that occultation did not provide a suitable profile for that wave.

Star	Rev		W80.98	W81.02	W82.00	W82.06	W82.21	W83.63	W84.64	W85.67	W87.19
R Hya	036	i	220948260. 174.°072	220948254. 174.°109	220948093. 175.°060	220948085. 175.°108	220948061. 175.°249	220947834. 176.°544	220947678. 177.°411	220947519. 178.°273	220947295. 179.°453
α Aur	041	i	227949007. 343.°813		227948789. 345.°077	227948779. 345.°137	227948748. 345.°316	227948458. 346.°944	227948260. 348.°019	227948061. 349.°077	227947783. 350.°513
γ Cru	071	i	266193414. 183.°104	266193408. 183.°109	266193267. 183.°241	266193260. 183.°248	266193238. 183.°267		266192888. 183.°579	266192738. 183.°707	266192521. 183.°886
γ Cru	073	i	267426088. 182.°136		267425942. 182.°281	267425934. 182.°288	267425913. 182.°309	267425709. 182.°506	267425565. 182.°641	267425415. 182.°778	267425200. 182.°969
γ Cru	077	i	269858216. 181.°086		269858071. 181.°240	269858064. 181.°247	269858043. 181.°269		269857698. 181.°619	269857550. 181.°763	269857336. 181.°965
γ Cru	078	i	270466692. 180.°860		270466548. 181.°015	270466541. 181.°023	270466520. 181.°045	270466318. 181.°255	270466175. 181.°398	270466028. 181.°544	270465815. 181.°747
β Gru	078	i							270512794. 302.°774	270512542. 298.°579	270512284. 294.°401
γ Cru	079	i	271045522. 179.°175		271045367. 179.°354	271045359. 179.°363	271045337. 179.°389		271044967. 179.°796	271044809. 179.°964	271044581. 180.°198
RS Cnc	080	i	271872473. 90.°240	271872458. 90.°145	271872088. 87.°858	271872070. 87.°749	271872018. 87.°431	271871557. 84.°679	271871263. 82.°976	271870979. 81.°365	
RS Cnc	080	e	271877226. 121.°515	271877241. 121.°610	271877611. 123.°897	271877629. 124.°005	271877681. 124.°324	271878142. 127.°075	271878435. 128.°778	271878720. 130.°388	
γ Cru	081	i	272320388. 178.°322	272320382. 178.°329	272320233. 178.°510	272320226. 178.°519	272320203. 178.°546	272319987. 178.°800	272319834. 178.°974	272319676. 179.°151	272319448. 179.°397
γ Cru	082	i	272956171. 177.°862	272956166. 177.°869	272956016. 178.°056	272956009. 178.°065	272955986. 178.°093		272955616. 178.°533	272955457. 178.°714	272955229. 178.°967
RS Cnc	085	i			275057262. 97.°236	275057224. 97.°000	275057119. 96.°337	275056348. 91.°565	275055930. 89.°056	275055553. 86.°845	275055073. 84.°114
RS Cnc	085	e			275059898. 114.°136	275059935. 114.°371	275060040. 115.°034	275060811. 119.°806	275061229. 122.°315	275061606. 124.°525	275062086. 127.°256
γ Cru	086	i	275503697. 176.°829	275503692. 176.°837	275503542. 177.°033	275503535. 177.°043	275503512. 177.°073			275502984. 177.°728	275502756. 177.°995
RS Cnc	087	i						276330567. 96.°181	276329996. 92.°695	276329532. 89.°925	276328974. 86.°701
RS Cnc	087	e						276333572. 115.°078	276334143. 118.°564	276334608. 121.°334	276335165. 124.°557
γ Cru	089	i	277408751. 176.°576	277408745. 176.°584	277408596. 176.°781	277408589. 176.°791	277408566. 176.°821		277408198. 177.°288	277408040. 177.°480	277407813. 177.°749
γ Cru	093	i	280045204. 208.°249	280045198. 208.°242	280045028. 208.°061	280045020. 208.°052	280044994. 208.°024		280044575. 207.°597	280044395. 207.°421	280044136. 207.°175
γ Cru	094	i	280681410. 191.°683		280681250. 191.°696	280681242. 191.°697	280681218. 191.°699		280680835. 191.°728	280680670. 191.°741	280680433. 191.°758
γ Cru	096	i	282014259. 185.°190	282014253. 185.°193	282014111. 185.°280	282014104. 185.°285	282014083. 185.°298	282013876. 185.°420	282013731. 185.°504	282013580. 185.°589	282013362. 185.°708
γ Cru	100	i	285034037. 224.°282		285033857. 223.°835	285033848. 223.°814	285033822. 223.°749		285033397. 222.°739	285033216. 222.°326	285032956. 221.°750
γ Cru	101	i	285861190. 224.°289	285861183. 224.°272	285861011. 223.°842	285861002. 223.°820	285860975. 223.°755		285860551. 222.°744	285860370. 222.°331	285860110. 221.°755
γ Cru	102	i	286686360. 223.°942	286686354. 223.°926	286686182. 223.°500	286686173. 223.°479	286686147. 223.°415		286685724. 222.°416	286685544. 222.°007	286685285. 221.°438
β Peg	104	i	288914432. 342.°574	288914429. 342.°591	288914336. 343.°021	288914332. 343.°042	288914318. 343.°107		288914090. 344.°115	288913993. 344.°528	
R Cas	106	i	291039691. 90.°705	291039659. 90.°524	291038969. 86.°728	291038939. 86.°566	291038853. 86.°097		291037728. 80.°176	291037338. 78.°210	291036830. 75.°723
α Sco	115	i	302022977. 157.°895	302022964. 157.°914	302022637. 158.°409	302022621. 158.°434	302022571. 158.°508			302021428. 160.°139	302020939. 160.°797
β Peg	170	e	397973362. 78.°465	397973371. 78.°478		397973608. 78.°837	397973643. 78.°888	397973970. 79.°366		397974439. 80.°022	397974782. 80.°482
β Peg	172	i	401620518. 312.°326	401620509. 312.°312	401620280. 311.°950	401620269. 311.°932	401620234. 311.°877	401619902. 311.°371	401619669. 311.°025	401619428. 310.°676	401619082. 310.°189
λ Vel	173	i								403833306. 147.°873	
α Lyr	175	i								406601709. 268.°044	

Table 2. *Continued.*

Star	Rev		W80.98	W81.02	W82.00	W82.06	W82.21	W83.63	W84.64	W85.67	W87.19
W Hya	179	i	411902978. 146.520	411902973. 146.494	411902841. 145.824	411902834. 145.791	411902814. 145.690			411902358. 143.508	
W Hya	180	i				413052249. 146.312	413052229. 146.210	413052038. 145.265	413051906. 144.625	413051769. 143.984	413051575. 143.097
W Hya	181	i	414201633. 147.135	414201628. 147.108	414201494. 146.422		414201467. 146.285	414201277. 145.336	414201144. 144.694	414201007. 144.051	
R Cas	185	i	418067466. 331.261			418067199. 330.441	418067162. 330.329			418066320. 327.890	418065965. 326.923
μ Cep	185	e		418015692. 44.302	418016089. 45.391	418016110. 45.445	418016169. 45.606	418016725. 47.076	418017105. 48.053	418017491. 49.019	418018032. 50.337
γ Cru	187	i	419919773. 151.851	419919766. 151.815	419919584. 150.890	419919575. 150.844	419919547. 150.707	419919290. 149.443	419919112. 148.597	419918931. 147.754	419918675. 146.597
γ Cru	187	e	419930501. 225.432	419930508. 225.468	419930689. 226.391	419930699. 226.438	419930726. 226.575	419930983. 227.836	419931160. 228.681	419931341. 229.522	419931596. 230.676
R Cas	191	i	423133316. 296.924	423133309. 296.917		423133127. 296.706	423133100. 296.676		423132671. 296.202	423132487. 296.007	
μ Cep	191	i			423056492. 290.148	423056481. 290.141			423055942. 289.828	423055724. 289.707	423055410. 289.538
μ Cep	193	i	425123419. 290.475		425123206. 290.342	425123195. 290.336	425123164. 290.316		425122656. 290.014	425122438. 289.890	425122124. 289.716
R Cas	194	e				426260018. 84.264			426260474. 84.782	426260659. 84.982	426260924. 85.262

5 W81.02, ANOTHER WAVE GENERATED A NORMAL MODE OSCILLATION?

Baillié et al. (2011) identified a rather weak feature in the middle C-ring that could potentially be generated by another planetary normal mode. They designated this feature with the number 14, but to be consistent with our existing notation and Colwell et al. (2009) we will call this wave W81.02 here. Fig. 5 shows a sample profile of this wave, compared with the profiles of two normal mode generated waves previously analysed by Hedman & Nicholson (2013). W81.02 is clearly much weaker than the other waves we have analysed. Indeed, it is difficult to discern whether this wave propagates inwards or outwards. Based on co-added data from multiple occultations, Baillié et al. (2011) infer that this is an outward-propagating wave, but given the feature's low signal-to-noise ratio, this finding is not as secure as it is for other waves in this region.

We considered both positive and negative values of m in our analysis of this wave. We found no clear minimum at the appropriate pattern speed for any positive value of m, but at least two negative values of m yielded a minimum near the expected pattern speeds. If we considered a radial range of 81 010–81 030 km and a wavelength range of 0.5–2.0 km, the deepest minimum was found with $m = -11$ (see Fig. 6). However, a weak minimum also exists for $m = -5$ (see Fig. 7). In principle, the relative depths of the two minima could be used to estimate the relative likelihood that either one of these solutions is correct. However, in practice the depths of the minima are sensitive to the ranges of wavelengths and radii considered in the analysis, which makes the relative statistical significance of these solutions difficult to quantify. Thus we will simply note that the dispersion in the phase residuals around the $m = -5$ solution is larger than it is for the $m = -11$ solution, and that the $m = -5$ solution is less robust against small changes in the ranges of wavelengths and radii considered in the analysis. Both of these considerations would lead us to favour the $m = -11$ solution, but we cannot definitively rule out the $m = -5$ solution at this point.

While our analysis was able to provide two potential solutions, at present we regard these identifications as extremely tentative. Not only is the signal-to-noise ratio of this feature extremely low and the dispersion in the phase residuals high, but we also cannot use the inferred surface mass density and resonance location to confirm the identity of this wave. A negative value for m implies that the feature is an inward-propagating wave, contradicting the Baillié et al. (2011) analysis. While Baillié et al. (2011) could have misidentified the wave as outward propagating on account of its low signal-to-noise ratio and limited radial extent, the lack of consistency between our findings means that we cannot use their estimates of the ring's opacity or surface mass density to confirm our estimate of m.

If we assume that W81.02 is generated by a fundamental sectoral normal mode inside Saturn, then the location of this feature could in principle help confirm its identification. According to Marley & Porco (1993), the locations of the sectoral normal modes follow a non-monotonic but well-defined trend that arises because both the predicted pattern speeds for the sectoral normal modes and the resonant pattern speeds for outer Lindblad resonances at a given radius decrease with increasing $|m|$. For m between 2 and 5, it turns out that the resonant locations shift inwards with increasing m from about 86 000 to 81 000 km. For higher values of m the resonant locations steadily move outwards with increasing m. The locations and pattern speeds of the other waves in this region follow this predicted trend (see Fig. 2). W81.02 falls just exterior to W80.98, which Hedman & Nicholson (2013) identified as an $m = -4$ wave, and interior to the $m = -10$ wave W83.63. Hence W81.02 falls close to the predicted resonance location for the $m = 5$ fundamental sectoral normal mode, and well interior to the predicted resonance location for the $m = 11$ normal mode. Such considerations would favour the $m = -5$ solution for this wave. However, this argument presupposes that this pattern should occur at one of the predicted resonant locations for fundamental sectoral normal modes. Even if this

Table 3. Observed times (in seconds of ephemeris time, measured from the J2000 epoch) and inertial longitudes (measured relative to the longitude of ascending node on the J2000 equator) for the occultation cuts through the various $m = +3$ waves. Blank entries indicate that occultation did not provide a suitable profile for that wave.

Star	Rev		W84.82	W84.86	W86.40 (inner)	W86.40 (outer)	W86.58	W86.59	Mimas 6:2	Pandora 4:2
R Hya	036	i	220947650.	220947643.	220947411.	220947406.	220947385.	220947382.	220946906.	220946903.
			177°.564	177°.602	178°.851	178°.875	178°.984	179°.000	181°.407	181°.421
α Aur	041	i	227948225.	227948217.	227947926.	227947920.	227947895.	227947891.	227947307.	227947304.
			348°.207	348°.254	349°.782	349°.811	349°.944	349°.963	352°.857	352°.873
γ Cru	071	i	266192862.	266192855.	266192633.	266192629.	266192609.	266192606.	266192133.	266192131.
			183°.601	183°.607	183°.794	183°.798	183°.814	183°.817	184°.193	184°.195
γ Cru	073	i	267425539.	267425532.	267425311.	267425307.	267425287.	267425284.	267424814.	267424811.
			182°.665	182°.671	182°.871	182°.874	182°.892	182°.895	183°.295	183°.297
γ Cru	077	i			269857447.	269857443.	269857423.	269857420.		
					181°.862	181°.866	181°.884	181°.887		
γ Cru	078	i	270466149.	270466143.	270465925.	270465920.	270465901.	270465898.		
			181°.424	181°.430	181°.643	181°.647	181°.666	181°.668		
β Gru	078	i	270512741.	270512729.	270512409.	270512404.	270512380.	270512377.		
			301°.891	301°.686	296°.395	296°.313	295°.935	295°.882		
γ Cru	079	i	271044940.	271044933.	271044699.	271044694.	271044673.	271044670.	271044172.	271044169.
			179°.826	179°.833	180°.078	180°.083	180°.104	180°.108	180°.598	180°.601
RS Cnc	080	i	271871212.	271871200.	271870791.	271870783.	271870748.	271870743.	271869972.	271869968.
			82°.684	82°.612	80°.321	80°.280	80°.086	80°.058	75°.991	75°.969
RS Cnc	080	e	271878486.	271878499.	271878908.	271878915.	271878951.	271878956.	271879726.	271879730.
			129°.070	129°.141	131°.432	131°.473	131°.667	131°.695	135°.761	135°.783
γ Cru	081	i	272319806.	272319799.	272319566.	272319561.	272319540.	272319537.	272319039.	272319036.
			179°.005	179°.013	179°.271	179°.275	179°.298	179°.302	179°.817	179°.820
γ Cru	082	i	272955588.	272955581.	272955347.	272955342.	272955321.	272955318.	272954819.	272954816.
			178°.565	178°.573	178°.838	178°.843	178°.866	178°.869	179°.400	179°.403
RS Cnc	085	i	275055861.	275055844.	275055313.	275055304.	275055260.	275055253.	275054331.	275054326.
			88°.646	88°.546	85°.471	85°.416	85°.166	85°.130	80°.087	80°.061
RS Cnc	085	e	275061298.	275061315.	275061846.	275061855.	275061899.	275061905.	275062828.	275062833.
			122°.725	122°.824	125°.899	125°.953	126°.204	126°.240	131°.281	131°.308
γ Cru	086	i		275503108.	275502874.	275502869.	275502848.	275502845.	275502347.	275502344.
				177°.579	177°.858	177°.863	177°.888	177°.892	178°.451	178°.454
RS Cnc	087	i	276329908.	276329887.	276329250.	276329239.	276329188.	276329181.	276328153.	276328147.
			92°.166	92°.039	88°.282	88°.218	87°.924	87°.882	82°.169	82°.139
RS Cnc	087	e	276334231.	276334252.	276334889.	276334900.	276334951.	276334958.	276335986.	276335992.
			119°.093	119°.220	122°.976	123°.040	123°.334	123°.376	129°.088	129°.118
γ Cru	089	i	277408171.	277408164.	277407931.	277407926.	277407905.	277407902.	277407406.	277407403.
			177°.322	177°.330	177°.611	177°.617	177°.641	177°.645	178°.207	178°.211
γ Cru	093	i	280044544.	280044536.	280044270.	280044265.	280044241.	280044238.	280043673.	280043670.
			207°.566	207°.558	207°.301	207°.296	207°.273	207°.270	206°.755	206°.752
γ Cru	094	i			280680556.	280680551.	280680529.	280680526.		
					191°.749	191°.749	191°.751	191°.751		
γ Cru	096	i	282013705.		282013475.	282013471.	282013451.	282013448.	282012973.	282012970.
			185°.519		185°.647	185°.649	185°.660	185°.662	185°.911	185°.912
γ Cru	100	i	285033365.	285033358.	285033091.	285033085.	285033061.	285033058.	285032494.	285032491.
			222°.666	222°.648	222°.045	222°.034	221°.980	221°.973	220°.775	220°.768
γ Cru	101	i	285860519.	285860511.	285860244.	285860239.	285860215.	285860211.	285859648.	285859644.
			222°.671	222°.653	222°.050	222°.038	221°.985	221°.977	220°.779	220°.772
γ Cru	102	i	286685692.	286685684.	286685418.	286685413.	286685389.	286685386.		
			222°.343	222°.326	221°.730	221°.718	221°.665	221°.658		
β Peg	104	i		288914069.	288913926.	288913923.	288913911.	288913909.	288913607.	288913605.
				344°.206	344°.808	344°.819	344°.872	344°.880	346°.075	346°.082
R Cas	106	i	291037657.	291037640.	291037086.	291037076.	291037029.	291037023.	291036027.	291036022.
			79°.815	79°.727	76°.965	76°.916	76°.687	76°.655	71°.974	71°.949
α Sco	115	i			302021191.	302021182.	302021136.	302021130.	302020071.	302020065.
					160°.460	160°.473	160°.534	160°.543	161°.910	161°.918
β Peg	170	e	397974243.	397974253.			397974644.	397974648.		
			79°.751	79°.765			80°.298	80°.304		
β Peg	172	i	401619627.		401619261.	401619254.			401618465.	401618460.
			310°.964		310°.439	310°.429			309°.362	309°.356
W Hya	179	i	411902470.	411902464.	411902265.	411902261.				
			144°.025	143°.998	143°.082	143°.065				
W Hya	180	i	413051882.	413051876.	413051675.	413051671.	413051653.	413051651.	413051233.	413051230.

Table 3. *Continued.*

Star	Rev		W84.82	W84.86	W86.40 (inner)	W86.40 (outer)	W86.58	W86.59	Mimas 6:2	Pandora 4:2
			144.°512	144.°484	143.°551	143.°533	143.°451	143.°439	141.°610	141.°599
W Hya	181	i	414201120.	414201114.	414200913.	414200909.	414200891.	414200889.	414200471.	414200468.
			144.°580	144.°552	143.°616	143.°598	143.°516	143.°504	141.°668	141.°658
R Cas	185	i	418066525.							
			328.°466							
μ Cep	185	e	418017173.	418017190.	418017754.	418017765.	418017815.	418017822.	418018966.	418018973.
			48.°225	48.°267	49.°666	49.°692	49.°814	49.°831	52.°503	52.°518
γ Cru	187	i	419919080.	419919073.	419918807.	419918802.	419918778.	419918775.	419918229.	419918226.
			148.°447	148.°410	147.°187	147.°164	147.°057	147.°042	144.°678	144.°664
γ Cru	187	e	419931192.	419931200.	419931465.	419931470.	419931494.	419931497.	419932041.	419932044.
			228.°830	228.°867	230.°087	230.°110	230.°217	230.°232	232.°590	232.°604
μ Cep	191	i	423055904.	423055895.	423055573.	423055567.	423055538.	423055533.	423054848.	423054844.
			289.°807	289.°802	289.°625	289.°621	289.°605	289.°603	289.°248	289.°246
μ Cep	193	i	425122618.	425122608.	425122286.	425122280.	425122251.	425122247.	425121561.	425121557.
			289.°993	289.°987	289.°806	289.°802	289.°786	289.°784	289.°420	289.°417
R Cas	194	e			426260787.	426260792.				
					85.°118	85.°124				

Table 4. Time, longitude and phase differences used to determine pattern speeds (full table included in on-line supplement).

Wave	Occultation pair	δt (d)	$\delta\lambda$ (°)	$\delta\phi$ (°)	σ_ϕ (°)
W82.00	RSCnc085e–RSCnc085i	0.03051	16.9	241.2	2.7
W82.06	RSCnc085e–RSCnc085i	0.03137	17.4	242.2	6.0
W82.21	RSCnc085e–RSCnc085i	0.03381	18.7	242.4	7.2
W83.63	RSCnc087e–RSCnc087i	0.03478	18.9	48.5	7.1
W84.64	RSCnc087e–RSCnc087i	0.04799	25.9	223.8	5.0

Table 5. Summary of wavelet analyses.

Wave	Resonant location[a] (km)	Region considered[b] (km)	Wavelengths considered[b] (km)	$N(\delta\phi)$[c]	m	Pattern speed (° d^{-1})	Rotation period (min)	σ_0 (g cm^{-2})	τ_n^a	τ_n/σ_0 (cm^2 g^{-1})
W80.98	80 998	80 970–80 995	0.1–5	193	−4	1660.4	312.2	5.85	0.13	0.022
W82.00	82 010	81 992–82 012	0.1–5	255	−3	1736.6	298.5	5.68	0.14	0.025
W82.06	82 061	82 040–82 065	0.1–5	286	−3	1735.0	298.8	10.16	0.28	0.028
W82.21	82 209	82 190–82 215	0.1–5	247	−3	1730.3	299.6	6.92	0.13	0.020
W83.63	83 633	83 625–83 635	0.1–5	63	−10	1394.1	371.9	4.95	0.10	0.020
W84.64	84 644	84 625–84 650	0.1–5	311	−2	1860.8	278.6	4.05	0.11	0.027
W84.82	84 814	84 810–84 830	1.0–5	218	+3	833.5	622.0	3.94	0.44	0.11
W84.86	84 857	84 850–84 880	1.0–5	146	+3	833.0	622.3	2.24	0.42	0.19
W85.67	85 677	85 675–85 690	1.0–5	300[d]	−1	2430.5	213.3	–	0.29	–
W86.40	86 400	86 400–86 420	1.0–5	179	+3	810.4	639.7	4.70	0.47	0.10
W86.58	86 576	86 575–86 585	1.0–5	121	+3	807.9	641.7	1.18	0.38	0.31
W86.59	86 590	86 595–86 605	1.0–5[e]	243	+3	807.7	641.8	–	–	–
W87.19	87 189	87 175–87 205	0.1–5	164	−2	1779.5	291.3	1.41	0.15	0.11

[a]From table 7 of Baillié et al. (2011).
[b]Radial range and wavelength range considered in wavelet analysis.
[c]Number of $\delta\phi$ values used in fit.
[d]Includes observations with δt as large at 1000 d.
[e]Data high-pass filtered prior to fitting.

wave is generated by such an oscillation, differential rotation could displace the predicted resonant locations inwards (Marley 1991). Barring more detailed models of the planet's internal oscillations, we cannot yet rule out the possibility that a $m = 11$ pattern could have a resonance near W81.02.

Since the dispersion in phase measurements favours the $m = -11$ solution, while its location could support the $m = -5$ option, it would be premature to categorize W81.02 as either pattern. Hence we do not list this feature in Table 5. However, this wave does merit further investigation with larger data sets and more refined

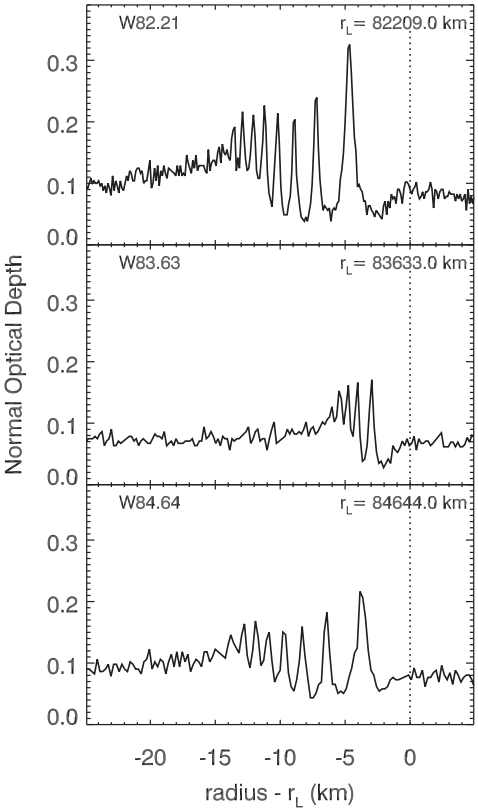

Figure 3. Sample Profile of W83.63, compared with two other inward-propagating waves in its vicinity. These profiles are from the egress portion of the Rev 85 RSCnc occultation ($B = 29.^{\circ}96$) which sampled all three waves relatively well. Hedman & Nicholson (2013) showed that W82.21 is likely an $m = -3$ wave, while W84.64 is probably an $m = -2$ wave. Note that W83.63 has a noticeably shorter wavelength than either of the other waves, but its opacity variations are close to saturation, like the other two waves.

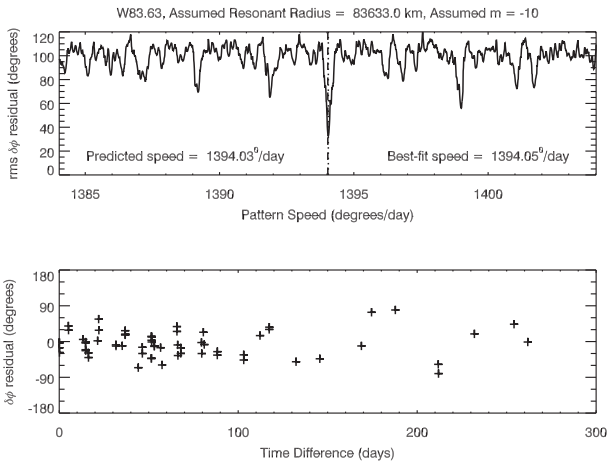

Figure 4. Results of a wavelet analysis of wave W83.63 which considered the radial range of 83 625–83 635 km and a pattern wavelength range of 0.1–5 km. The top panel shows the rms phase difference residuals as a function of pattern speed, assuming the wave is an $m = -10$ pattern. The dashed line marks the expected pattern speed for such a structure with the appropriate resonant radius, while the dotted line indicates the best-fitting pattern speed. There is a clear minimum in the residuals very close to the predicted location (other minima are likely aliasing within the sparse data set). The bottom panel shows the phase difference residuals (observed − expected) for this best-fitting solution as a function of time difference between the observations. Note the scatter in the residuals is around 45°.

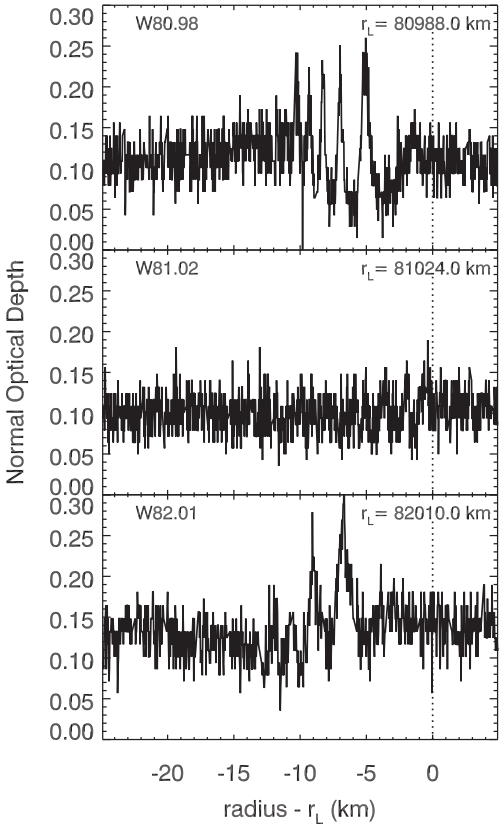

Figure 5. Sample profile of W81.02, compared with two other inward-propagating waves in its vicinity. These profiles are from the Rev 106 RCas occultation ($B = 56.^{\circ}04$) which sampled all three waves relatively well. Hedman & Nicholson (2013) showed that W80.98 is likely an $m = -4$ wave, while W82.01 is probably an $m = -3$ wave. Note that Baillié et al. (2011) identified W81.02 as an outward-propagating wave with a resonance location around 81 018 km. To facilitate comparisons, we here plot the wave as if it were an inward-propagating wave initiated at 81 024 km. This wave is clearly much weaker than the other two, and the wavelength trend with radius is ambiguous.

analytical methods, since it could represent another resonance with planetary normal mode oscillations.

6 MULTIPLE $m = +3$ WAVES IN THE OUTER C-RING

Besides W81.02, seven of the weak waves discovered by Baillié et al. (2011) were detectable in individual VIMS occultations profiles. These were designated features 20, 21, 28, 29, 31, 36 and 37 by Baillié et al. (2011), who suggested that the outermost two of these features are generated by the Mimas 6:2 and Pandora 4:2 inner Lindblad resonances at 89 883 and 89 894 km, respectively. They also point out that feature 20 is only a few kilometres from the Pan 4:2 inner Lindblad resonance, but the distance between the wave and the resonance, along with lack of an obvious wave at the much stronger 2:1 resonance, strongly suggests that this is just a coincidence. Hence Baillié et al. (2011) conclude that the inner five waves have no known resonance that could explain them. To be consistent with the nomenclature of other unknown features (Colwell et al. 2009), we will here designate these features as waves W84.82, W84.86, W86.40, W86.58 and W86.59 [the nominal resonant locations of the inner four features are 84 814, 84 857, 86 400 and

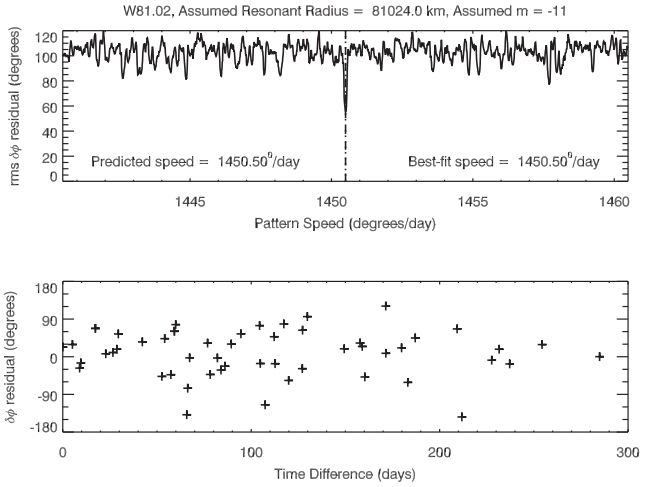

Figure 6. Results of a wavelet analysis of wave W81.02 which considered the radial range of 81 010–81 030 km and a pattern wavelength range of 0.5–2 km. The top panel shows the rms phase difference residuals as a function of pattern speed, assuming the wave is an $m = -11$ pattern. The dashed line marks the expected pattern speed for such a structure with the appropriate resonant radius. There is a minimum in the residuals very close to the predicted location. The bottom panel shows the phase difference residuals (observed − expected) for this best-fitting solution as a function of time difference between the observations.

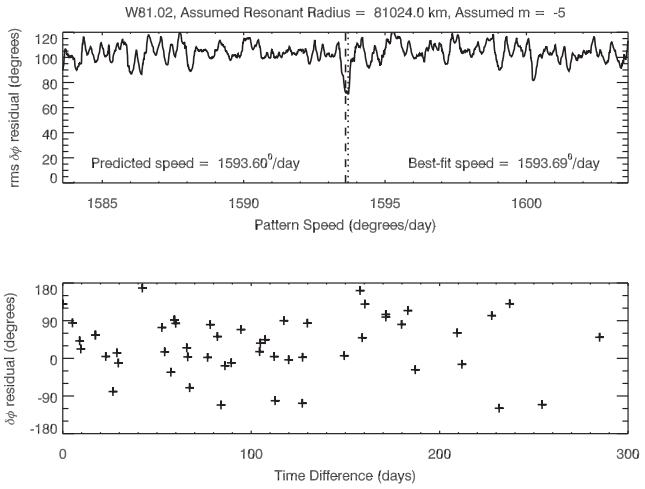

Figure 7. Results of a wavelet analysis of wave W81.02 which considered the radial range of 81 010–81 030 km and a pattern wavelength range of 0.5–2 km. The top panel shows the rms phase difference residuals as a function of pattern speed, assuming the wave is an $m = -5$ pattern. The dashed line marks the expected pattern speed for such a structure with the appropriate resonant radius. There is a weak minimum in the residuals close to the predicted location. The bottom panel shows the phase difference residuals (observed − expected) for this alternate solution as a function of time difference between the observations.

86 576 km, respectively, according to Baillié et al. (2011), while the last feature appears to have a resonant radius around 86 590 km].

Fig. 8 shows sample profiles of these seven waves. While some periodic structures are visible at these locations, the signal-to-noise ratio of these features is much lower than it was for the waves considered by Hedman & Nicholson (2013). This is not only because the amplitudes of the waves themselves are smaller, but also because they occupy sharp-edged regions of enhanced optical depth known as plateaux (see Fig. 1). These regions show enhanced fine-

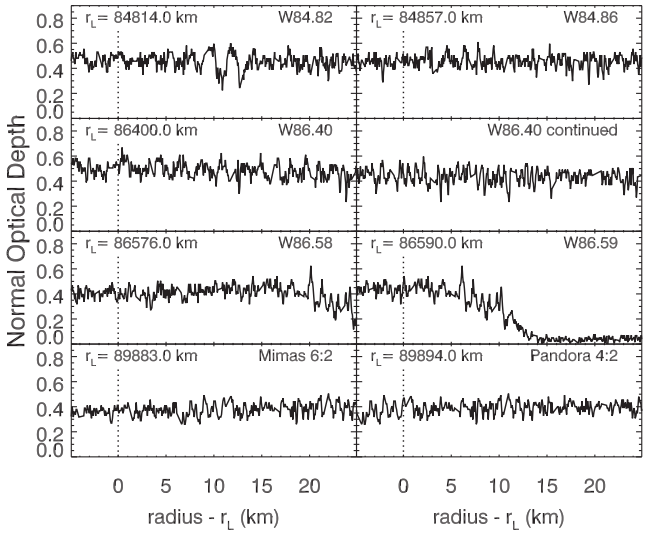

Figure 8. Sample profiles of seven C-ring waves from the Rev 106 RCas occultation ($B = 56.^{\circ}04$). Vertical dotted lines indicate the resonant radii, as fitted by Baillié et al. (2011). Note that these waves are all found in plateaux, and have much lower signal-to-noise ratio than the waves illustrated in Fig. 3. Still, quasi-periodic patterns with wavelengths around 1 km can be seen extending outwards of all the marked locations.

scale stochastic optical depth variations compared with the lower optical depth parts of the C-ring, and this fine-scale structure further obscures the waves. By combining wavelet data from multiple occultations, Baillié et al. (2011) found that, unlike the waves analysed by Hedman & Nicholson (2013), all of these waves appear to propagate *outwards*. Assuming these features are density waves,[5] this implies that their pattern speeds are slower than the local mean motion. Hence they are likely driven by inner Lindblad resonances and should all have a positive m-values.

Table 3 provides a list of the occultations with sufficient resolution and coverage to yield decent phase information on these waves. While the numbers of occultations available are comparable to those used in our earlier analyses of other waves, it was not immediately clear if our algorithms could provide robust estimates of pattern speeds and symmetry properties for such low amplitude features. Fortunately, we can actually test our algorithms using the two features Baillié et al. (2011) attribute to the 6:2 Mimas and 4:2 Pandora Lindblad resonances, both of which are located in Plateau P10 between 89 800 and 89 900 km. If these identifications are correct, then we would expect both these structures to be $m = +3$ patterns with the appropriate pattern speeds. Note that these two satellite-induced waves are even more obscure than the unidentified structures, and so they provide a stringent test of our algorithms' ability to isolate wave-like patterns from noisy data.

Figs 9 and 10 show the results of our wavelet analysis for both of these waves. We find that each wave does indeed yield a minimum

[5] While vertical bending waves with pattern speeds faster than the local mean motion would also propagate outwards (Shu 1984), the observed properties of the waves discussed here are not consistent with bending waves. The apparent optical depth contrast of vertical structures like bending waves depends on the elevation angle of the line-of-sight to the star through the ring plane, but the appearance of these waves exhibits no obvious trends with elevation angle. Also, the pattern speeds of density and bending waves are quite different, and the best-fitting pattern speeds of these features are consistent with density waves.

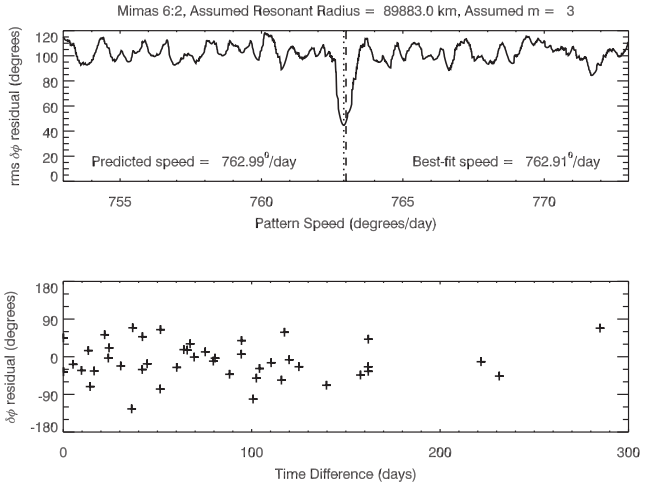

Figure 9. Results of a wavelet analysis of the wave near the Mimas 6:2 resonance which considered the radial range of 89 880–89 900 km and a wavelength range of 0.5–5 km. The top panel shows the rms phase difference residuals as a function of pattern speed, assuming the wave is an $m = +3$ pattern. The dashed line marks the expected pattern speed for the Mimas 6:2 inner Lindblad resonance (e^3 type). There is a clear minimum in the residuals very close to the predicted location. The bottom panel shows the phase difference residuals (observed − expected) as a function of time difference between the observations for this best-fitting solution.

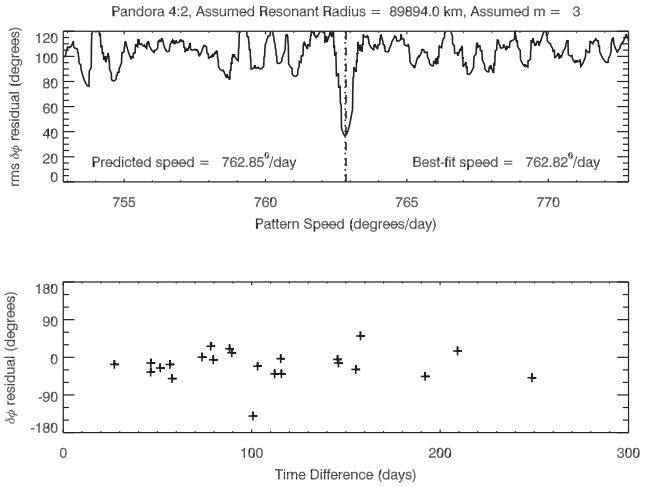

Figure 10. Results of a wavelet analysis of the wave near the Pandora 4:2 resonance which considered the radial range of 89 900–89 920 km and a wavelength range of 0.5–5 km. The top panel shows the rms phase difference residuals as a function of pattern speed, assuming the wave is an $m = +3$ pattern. The dashed line marks the expected pattern speed for the Pandora 4:2 inner Lindblad resonance. There is a clear minimum in the residuals very close to the predicted location. The bottom panel shows the phase difference residuals (observed − expected) as a function of time difference between the observations for this best-fitting solution.

in the rms phase difference residuals near the expected pattern speed when we assume that $m = +3$.[6] The rms dispersions of the residuals for these best-fitting models are not as good as they are for the waves considered by Hedman & Nicholson (2013), most likely because

[6] Note that since these are not first-order waves, the pattern speed does not equal the moon's orbital speed. Instead we have for the Pandora 4:2 resonance $\Omega_P = (4n_{Pandora} - \dot{\varpi}_{Pandora})/3 = 762.^{\circ}852\ d^{-1}$, while for the Mimas 6:2 resonance $\Omega_p = (6n_{Mimas} - 3\dot{\varpi}_{Mimas})/3 = 762.^{\circ}988\ d^{-1}$.

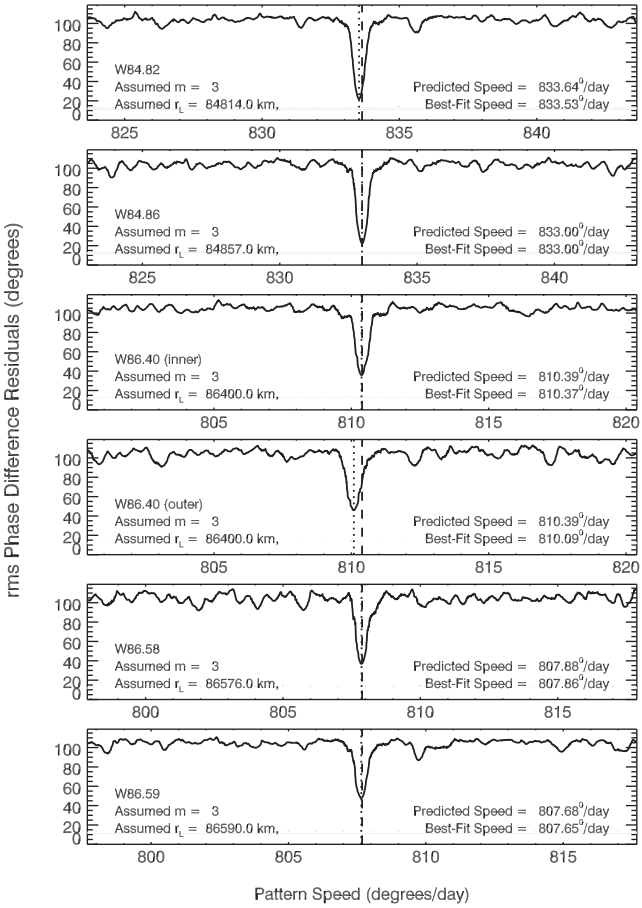

Figure 11. Plots showing the rms phase difference residuals as a function of pattern speed for the unidentified waves within plateaux P5 and P7, assuming $m = +3$ and using a wavelength range of 1–5 km for all cases except for the outer part of W86.40, which used a wavelength range of 0.3–1 km. The dashed lines mark the predicted pattern speed for each wave at the resonant location provided by Baillié et al. (2011), while the dotted lines are the pattern speeds that give the minimum variance in the residuals. Baillié et al. (2011) did not provide a resonance location for W86.59, and so here the predicted resonance location has been chosen to match the observed pattern speed.

of their relatively low signal-to-noise ratio. Even so, the minima are clear, and there are no similar minima near the expected pattern speeds for other values of m. Thus our methods do seem to be able to identify the correct m-numbers and pattern speeds of waves even in the presence of a noisy background. Furthermore, we can now confirm the tentative wave identifications made by Baillié et al. (2011).

Turning to the unidentified waves (W84.82, W84.86, W86.40, W86.58 and W86.59), we were surprised to find that all five of these patterns also showed clear minima when we assumed $m = +3$. As shown in Figs 11 and 12, the best-fitting models for these waves typically have smaller residuals than those derived above for the Mimas 6:2 and Pandora 4:2 waves. This probably reflects the somewhat higher visibility of these waves in the individual profiles.

Waves W84.82 and W84.86 both inhabit the same plateau P5, and are only 35 km apart (see Fig. 1). We computed the phase differences for these waves using the radial ranges 84 810–84 830 and 84 850–84 880 km. We only considered wavelengths between 1 and 5 km for these waves in an effort to minimize any contamination from

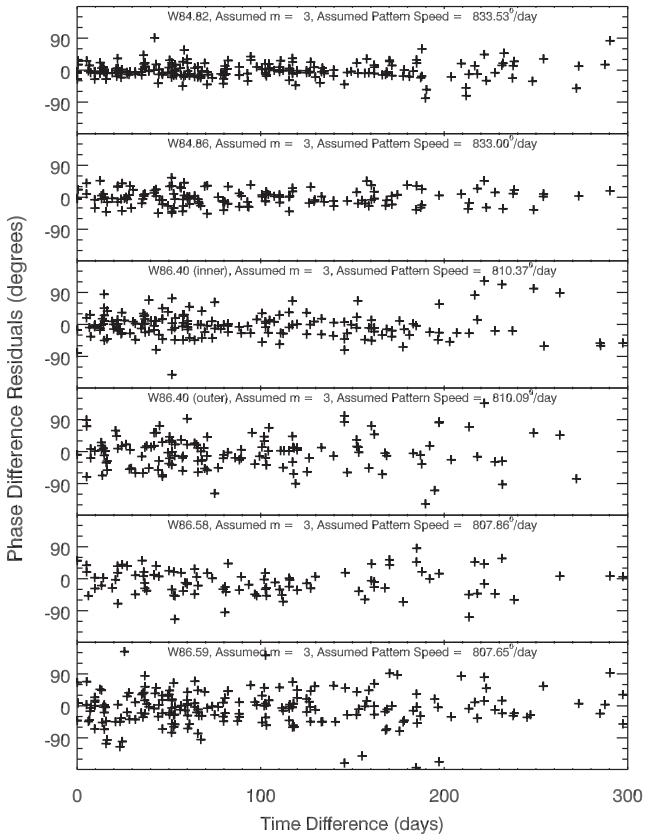

Figure 12. Plots showing phase difference residuals (observed − predicted) for each of the waves, assuming each pattern has the indicated m-number and pattern speed, which correspond to the best-fitting values shown in Fig. 11.

fine-scale stochastic structure in this region. Fig. 11 shows that there is a clear minimum in the rms residuals for W84.82 when $m = +3$ and $\Omega_p = 833.^\circ53$ d^{-1}, or just $0.^\circ12$ d^{-1} slower than the expected pattern speed using the resonant radius of 84 814 km provided by Baillié et al. (2011), which is actually the predicted radius for the nearby 4:2 Pan resonance. This slight shift would imply the actual resonant location is 8 km exterior to this reported position, or around 84 822 km. This number is not unreasonable given that the prominent density variations start at about this location (see Fig. 8), and provides further evidence that this wave is not generated by the Pan resonance. Wave W84.86, on the other hand, shows a minimum for $m = +3$ and $\Omega_p = 833.^\circ00$ d^{-1}, which perfectly matches the expected pattern speed using the resonant radius of 84 857 km provided by Baillié et al. (2011). Note that the difference between these two pattern speeds is significant even if we consider only time separations up through 300 d. Thus we have two waves with the same symmetry properties and very similar, but not identical, pattern speeds.

Turning to wave W86.40, which is located in plateau P7, we first note that this wave seems to extend further from the putative resonance than W84.82 and W84.86 do. Furthermore, many profiles show hints of strong subkilometre wavelength structures 30–50 km exterior to the resonance. The wavelet analysis of Baillié et al. (2011) indicates that all these variations could potentially be ascribed to a single extensive wave, but to be sure, we decided to analyse the two parts of the wave separately, using radial ranges of 86 400–86 420 and 86 430–86 450 km for the inner and outer part, respectively. We continued to use the wavelength range of 1–5 km for the inner part of the wave, but we used 0.1–3 km for the outer part in order to capture the finer scale structure further from the resonance. As shown in Fig. 11, the inner part of the wave yields a clear $m = +3$ pattern with a pattern speed of $810.^\circ37$ d^{-1}, which matches the expected value for the resonant radius of 86 400 km derived by Baillié et al. (2011). Intriguingly, the outer part of the wave also shows a minimum when we assume $m = +3$, but at a slightly slower pattern speed of $810.^\circ09$ d^{-1} (this difference in pattern speed remains even if we use the same wavelength range for both parts of the wave). The residuals for the outer part of the wave have a larger scatter, which probably reflects the shorter wavelength of the pattern in this region. The slightly slower best-fitting pattern speed, which corresponds to a resonant radius of 86 418 km, could just represent systematic errors in the analysis due to the short wavelengths involved, but it could potentially indicate that there are actually two overprinted $m = +3$ waves occupying this region.

Baillié et al. (2011) identified three additional features (29–31) in the outer part of plateau P7. When we inspected the VIMS profiles, we could only discern two waves, which we designate W86.58 and W86.59. Baillié et al. (2011) provided a resonance location of 86 576 km for W86.58, but did not provide a resonant radius for W86.59. The latter feature overlaps the outer edge of the plateau (see Fig. 8), which would complicate the interpretation of any wavelength trends. When we analysed W86.58 using a radial range of 86 575–86 585 km and a wavelength range of 1–5 km, we obtained a reasonably clear minimum in the phase difference residuals with $m = +3$ and a pattern speed close to the predicted rate of $807.^\circ88$ d^{-1} (see Fig. 11). For W86.59, we considered a radial range of 86 595–86 605 km and a wavelength range of 1–5 km, but the sharp background slope contaminated the phase measurements. We therefore applied a high-pass filter to these data by subtracting a copy of the profile smoothed by a boxcar average with length 2 km. Phase differences derived from these filtered light curves yielded a clear minimum in the phase difference residual with $m = +3$ and a pattern speed of $807.^\circ65$ d^{-1}, consistent with the location of this wave. Note the rms scatters in the phase difference residuals are larger for these two waves than they are for W84.82 and W84.86 (see Fig. 12), most likely because of their lower signal-to-noise ratio.

It is remarkable that we have at least five $m = +3$ waves with pattern speeds between 807° and 834° d^{-1}. These pattern speeds do not correspond to the oscillation frequencies of planetary normal modes such as those computed by Marley & Porco (1993) or Marley (2014). Instead, they are close to Saturn's rotation rate. Saturn's magnetic dipole is almost perfectly aligned with its rotation axis, so its internal rotation rate is still uncertain, with various indirect estimates given rotation rates between 817° and 820° d^{-1} (Anderson & Schubert 2007; Read et al. 2009). On the other hand, the clouds in Saturn's atmosphere rotate around the planet at rates ranging between 808° and 828° d^{-1} at mid-latitudes, and up to 850° d^{-1} in the equatorial jet (García-Melendo et al. 2011; Sánchez-Lavega et al. 2014), while various periodic phenomena in Saturn's magnetosphere like the Saturn kilometric radiation (SKR) exhibit at least two components with frequencies ranging between 795° d^{-1} and 820° d^{-1} over the last few years (Ye et al. 2010; Lamy 2011; Andrews et al. 2012; Provan et al. 2013). Table 6 compares our observed pattern speeds for the $m = +3$ waves with a number of published estimates of rotation rates for various features in the planet's atmosphere, while Fig. 13 compares our pattern speeds with both the variable frequencies of the magnetospheric phenomena and Saturn's winds. Intriguingly, the pattern speeds of waves W86.40, W86.58 and W86.59 are close to the magnetospheric frequencies and Saturn's westward jets, while the pattern speeds of W84.82 and W84.86 are close to the rotation rate of Saturn's eastward jets.

Table 6. Pattern speeds of selected atmospheric phenomena, modified from Cowley & Provan (2013).

Phenomena	Rotation period (h)	Pattern speed ($^\circ$ d^{-1})	Reference
W84.82	10.365	833.5	This work
W84.86	10.372	833.0	This work
Estimate of bulk rotation from occultations	10.543	819.5	Anderson & Schubert (2007)
Estimate of bulk rotation from potential vorticity	10.570	817.4	Read, Dowling & Schubert (2009)
IAU System III	10.656	810.8	Davies et al. (1983)
North Polar Hexagon	10.656	810.8	Sánchez-Lavega et al. (2014)
W86.40	10.662	810.4	This work
Great White Spot Vortex	10.667	810.0	Sayanagi et al. (2013)
String of Pearls	10.686	808.5	Sayanagi et al. (2014)
Great White Spot Head	10.693	808.0	Sayanagi et al. (2013)
W86.58	10.695	807.9	This work
W86.59	10.698	807.7	This work

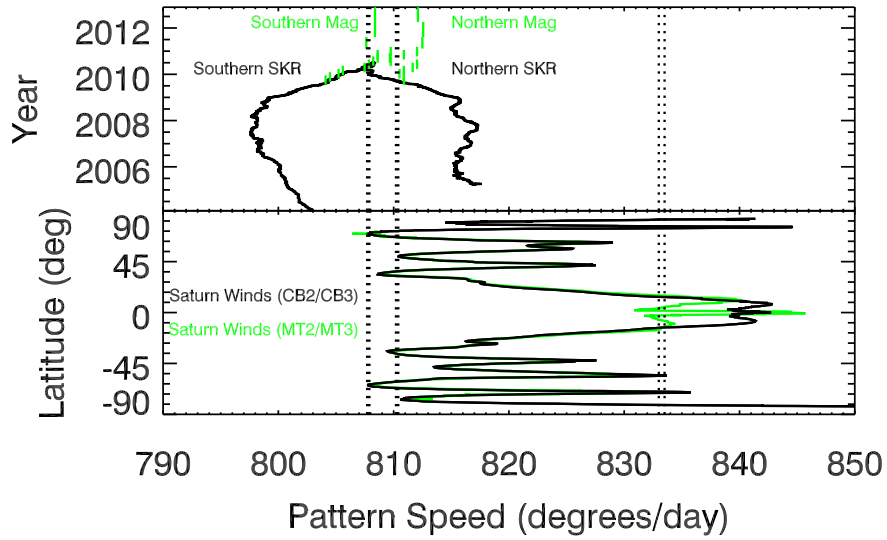

Figure 13. Comparing the pattern speeds of the $m = +3$ waves with the rotation rate of Saturn. In both panels above, the dotted lines mark the pattern speeds of the five $m = +3$ waves. The top panel compares these pattern speeds with the estimates of the SKR rotation rates during the first 7 yr of the *Cassini* mission (Lamy 2011), and the planetary period oscillations in the magnetic field (Provan et al. 2013). The bottom panel shows the rotation rates of Saturn's winds as a function of latitude from García-Melendo et al. (2011). Note the rotation rates of Saturn's equatorial jet depends on whether the images examined were obtained in continuum (black) or methane-band (green) filters.

Given the similarity between these wave's pattern speeds and Saturn's atmospheric and magnetospheric rotation rates, it seems likely that all of these waves are generated by 'tesseral' resonances with structures rotating with the planet. Such resonances were first suggested by Franklin, Colombo & Cook (1982) but turned out to be undetectable in the *Voyager* data (Holberg, Forrester & Lissauer 1982). The waves visible in the *Cassini* data all have $m = +3$, and occur where the Keplerian mean motion is around 3/2 Saturn's rotation rate, so they would all represent 3:2 tesseral resonances. This is sensible, because in the C-ring only $m = +3$ resonances have pattern speeds that can match the planet's rotation rate (see Fig. 2). However, different tesseral resonances could occur in other parts of the rings. Indeed, there are several patterns in both the D-ring and Roche Division which appear to be generated by resonances with multiple periodic perturbations with effective pattern speeds around 800° and 820° d^{-1} (Hedman et al. 2009), and these may correspond to the 2:1 and 3:4 tesseral resonances, respectively. In addition, the dusty spokes that form close to the planetary corotation radius also exhibit periodicities that have been tied to Saturn's rotation rate (Porco & Danielson 1982; Porco 1983; Mitchell et al. 2013). However, all of these previously studied structures involve ring material composed primarily of micron-sized particles. These tiny grains are very sensitive to non-gravitational forces and thus might be influenced by the same electromagnetic phenomena that modulate the SKR. The C-ring waves, by contrast, involve much denser rings composed of pebble-to-boulder-sized ice particles, and thus are almost certainly generated by periodic gravitational perturbations. These waves presumably trace long-lived gravitational anomalies inside Saturn that are carried around the planet by winds moving at slightly different rates.

In principle, the masses associated with these anomalies can be estimated from the waves' amplitudes. In practice, precise mass estimates would require detailed measurements of the wave profiles and assumptions about the spatial form of the anomaly, and such analyses are beyond the scope of this report. However, we can derive order-of-magnitude estimates of the perturbing masses by simply noting that the amplitudes of the relevant waves are comparable to those generated by the Mimas 6:2 and Pandora 4:2 resonances. The perturbations applied to the rings by these two satellite resonances are proportional to Me^p, where M is the moon's mass, e is its orbital

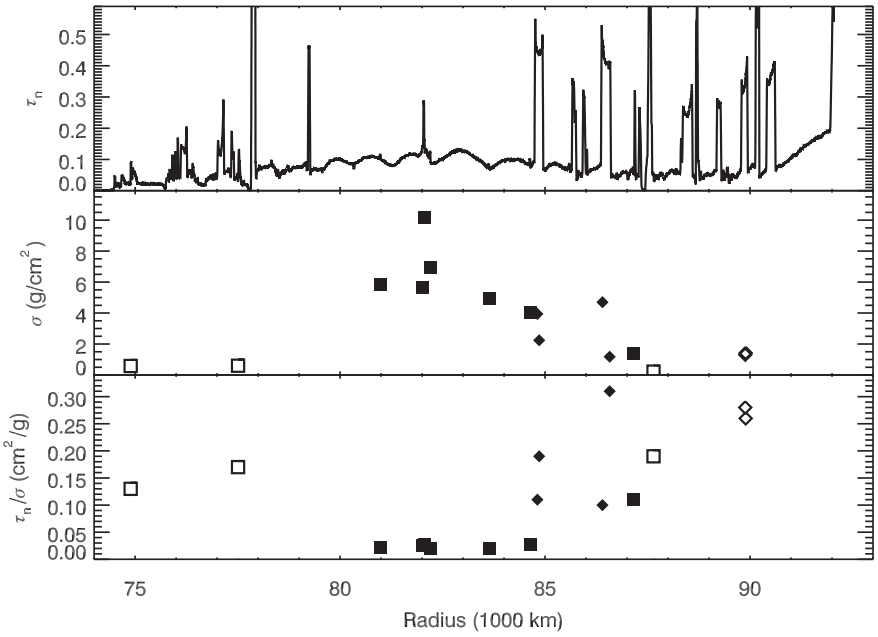

Figure 14. Comparisons of the C-ring's normal optical depth and surface mass density. The top panel shows an optical depth profile derived from the Rev 89 γ Crucis occultation. The centre and bottom panels show the surface mass density and opacity of the ring derived from various density waves. The open symbols are values derived by Baillié et al. (2011), while filled symbols utilize the m-values derived in this work and Hedman & Nicholson (2013). Squares represent waves in the background C-ring, while diamonds correspond to measurements in plateaux. Note that the ring's surface mass reaches a maximum and the opacity is at a minimum in the middle of the C-ring.

eccentricity and $p = 3$ for the Mimas 6:2 resonance while $p = 1$ for the Pandora 4:2 resonance. Numerically, these factors are 3×10^{14} and 6×10^{14} kg for the Mimas 6:2 and Pandora 4:2 resonances, respectively. If the unidentified $m = +3$ waves are generated by compact mass anomalies inside the planet, those masses would need to be of the same order as these factors to produce waves with similar amplitudes (neglecting various coefficients of order unity). Hence each wave would require a mass anomaly of order 10^{14}–10^{15} kg to generate the observed waves. This is comparable to the mass of a kilometre-sized icy satellite, and corresponds to a very small perturbation in the planet's density:

$$\frac{\delta\rho}{\rho_{\rm d}} \simeq 10^{-11} \left(\frac{0.7\,{\rm g\,cm^{-3}}}{\rho_{\rm d}}\right) \left(\frac{R_{\rm s}^3}{V_{\rm d}}\right), \quad (5)$$

where $\rho_{\rm d}$ and $V_{\rm d}$ are the mean mass density and volume of the region in the planet responsible for the mass anomaly. If the anomaly corresponds to a large-scale $m = 3$ perturbation in the planet's envelope, then $V_{\rm d}$ will be of order $R_{\rm s}^3$ and the density perturbation may be only one part in 10^{11}. However, if the anomalies are associated with something comparable in scale to Saturn's storm clouds (∼2000 km; Dyudina et al. 2007), then the density contrast could be more like 10^{-6}.

Unless these anomalies have a pure $m = 3$ structure inside the planet, we would expect additional gravitational tesseral resonances to be found elsewhere in the Main Rings. Thus far, no waves generated by tesseral resonances have been found outside the C-ring, but this may be because the 3:2 tesseral resonances are the ones that lie closest to the planet (excluding the 2:1 resonances, which fall in the D ring), and so produce the strongest perturbations on the ring material. However, careful searches for unidentified waves elsewhere in the B and A rings may eventually reveal additional examples.

Regardless of the source of these waves, their identification as $m = +3$ patterns exacerbates a pre-existing incongruity in the estimated mass densities of the plateaux. Again, using the estimates of $\sigma_0/|m - 1|$ and $\tau_{\rm n}/\sigma_0|m - 1|$ from Baillié et al. (2011), we find surface mass densities of 3.94, 2.24, 1.18 and 4.70 g cm^{-2} and opacities of 0.11, 0.19, 0.10 and 0.31 cm^2 g^{-1} for W84.82, W84.86, W86.40 and W86.58, respectively [see Table 5; as mentioned above, Baillié et al. (2011) did not provide mass density estimates for W86.59]. These mass density estimates are surprising because they are slightly less than those of the middle C-ring, even though the normal optical depths of these plateaux are several times larger (see Fig. 14). This indicates that the substantially larger optical depths found in the plateaux do not correspond to a similarly elevated mass density. Instead, it appears that the mass density of the C-ring peaks at around 82 000 km, and the plateaux have a comparable mass density to nearby lower optical depth portions of the ring. Indeed, the nearby waves W84.64 (in the background ring) and W84.82 (on a plateau) yield nearly the same mass density, even though their optical depths differ by a factor of 4.

Another way to look at these variations is to consider the opacity parameter $\tau_{\rm n}/\sigma_0$, which is inversely proportional to the effective mean particle size and average particle density. As shown in Fig. 14 and Table 5, the C-ring's opacity is at a minimum in the middle C-ring, and is substantially larger within the plateaux. In particular, the opacity from W84.82 is roughly four times larger than W84.64. Such rapid variations in the ring's opacity indicate that the average sizes and/or internal densities of particles in the plateaux differ dramatically from those in the rest of the C-ring. Data from *Cassini* radio occultations do indicate that there are substantial variations in the particle size distribution across the C-ring, but the trends found by those experiments only seem to further confuse the situation. Simultaneous measurements made at multiple radio wavelengths reveal that the background C-ring has a 30 per cent higher optical

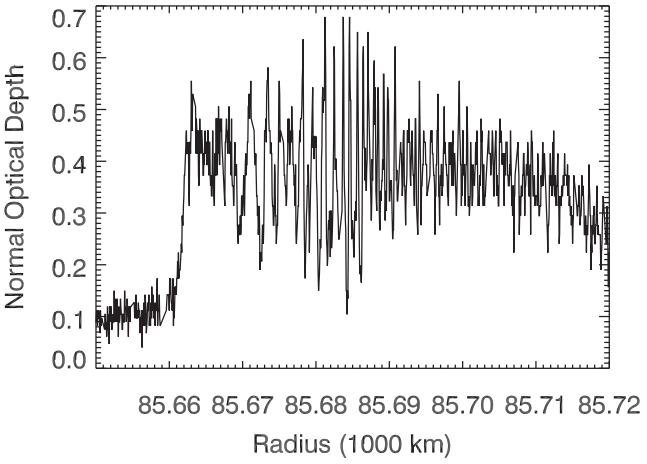

Figure 15. Sample profile of the W85.67 wave from the Rev 106 RCas occultation ($B = 56.^{\circ}04$). Note that this wave occupies a 100 km wide plateau known as P6, and its wavelength clearly decreases with increasing radius.

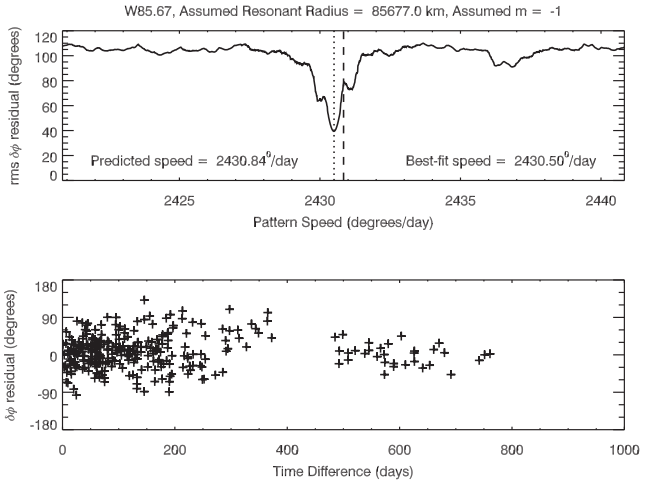

Figure 16. Results of a wavelet analysis of wave W85.67 which considered the radial range of 85 675–85 690 km and a wavelength range of 1–5 km. The top panel shows the rms phase difference residuals as a function of the assumed pattern speed, assuming the wave is an $m = -1$ pattern. The dashed line marks the expected pattern speed for such a structure with the resonant radius estimated by Baillié et al. (2011). There is a clear minimum in the residuals very close to the predicted location. The bottom panel shows the phase difference residuals (observed − expected) as a function of time difference between the observations for the best-fitting solution.

depth to 3.6 cm radiation than it does to 13.0 cm radiation, while this difference is much reduced in the plateaux (Cuzzi et al. 2009). This suggests that the middle C-ring has a larger fraction of centimetre-sized particles than the plateaux do, which implies that the particles in the plateaux are somewhat *larger* on average than the particles elsewhere in the C-ring.[7] This is problematic because larger particles have lower surface-area-to-volume ratios and so we should expect regions with larger typical particle sizes to have lower opacities, which is exactly the opposite of what we observe. Perhaps there are significant differences in the ring-particles' composition and/or internal mass density between these two regions. Ongoing analyses of *Cassini* occultation measurements, which indicate that there are also differences in the upper end of the particle size distributions between the plateaux and the background ring (Colwell et al. 2011; Colwell et al., in preparation), may help to clarify this situation.

7 W85.67, A MIGRATING $m = -1$ WAVE?

The final, and perhaps most perplexing, wave we will consider here was designated W85.67 by Colwell et al. (2009) [also known as wave *d* in Rosen et al. (1991) and feature 27 in Baillié et al. (2011)]. This wave lies between the W84.86 and W86.40 waves discussed above, and also occupies a plateau (P6, see Fig. 1). Compared with the $m = +3$ waves, however, this feature has much more prominent and obvious opacity variations (see Fig. 15). Its wavelength appears to decrease with increasing radius, which suggests that this is also an outward-propagating wave with a positive m-number. Table 2 lists the occultation profiles considered in this study. Since we must again contend with elevated levels of stochastic fine-scale structure in this region, we consider only wavelengths between 1 and 5 km, but our results are insensitive to the exact range.

We searched for patterns with $m = +1$ through $m = +15$ but did not find a clear minimum in the rms phase difference residuals within 10 d^{-1} of any of the expected pattern speeds. Out of desperation, we considered negative values of m,[8] and to our surprise found a strong minimum near the expected pattern speed when we used $m = -1$. This solution is shown in Fig. 16, which considers phase differences from occultations up to 1000 d apart in order to demonstrate that this solution is consistent with a steady pattern speed of $2430.^{\circ}5$ d^{-1}. We note that the dispersion around this best-fitting solution is rather large compared to the other unknown waves, but still all the phase difference residuals are within $\pm 90^{\circ}$ of zero, even with time separations approaching 1000 d.

An $m = -1$ solution for this wave is puzzling because the Ω_p implies an outer Lindblad resonance driven by a perturbation period of order 3 h, while the morphology of the wave is similar to outward-propagating waves driven by inner Lindblad resonances with moons. Furthermore, the derived pattern speed is actually somewhat slower than we might have expected. If this is a density wave with a resonant radius of 85 677 km (as derived by Baillié et al. 2011) we would instead predict a pattern speed of $2430.^{\circ}85$ d^{-1}, about $0.^{\circ}35$ d^{-1} faster than the observed value. To match the observed pattern speed, the resonant radius would need to be around 85 685 km, which lies within the wave itself. Such a discrepancy between the inferred resonant location of the wave has not been observed in any of the other waves we have examined, and reinforces the idea that something is odd about this wave.

Given these unusual observations, we decided to check our result by looking at the profiles themselves. Fig. 17 shows selected profiles, sorted by the predicted phase ϕ if we assume an $|m| = 1$ pattern rotating at $2430.^{\circ}5$ d^{-1}. We clearly see the spiral pattern where the peaks in optical depth shift systematically inwards with increasing phase, as expected for a trailing spiral. Thus the best-fitting $m = -1$ solution does indeed organize the data sensibly.

[7] Note that microwave measurements are sensitive primarily to particles in the centimetre to decametre size range.

[8] We also considered $m = 0$, which corresponds to a pattern with no azimuthal variations but a temporal oscillation frequency equal to the local radial epicyclic frequency. This case also failed to yield a sensible solution.

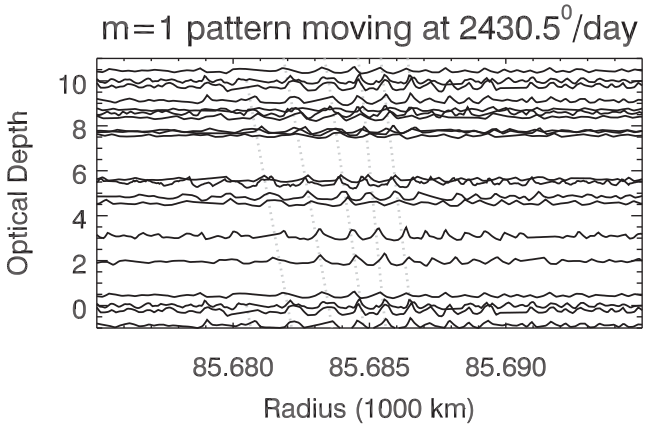

Figure 17. Selected profiles of the W85.67 wave versus radius, with vertical offsets proportional to the estimated phase of the pattern assuming $|m| = 1$ and $\Omega_p = 2430\overset{\circ}{.}5\ \mathrm{d}^{-1}$. Note that the same set of profiles is repeated near the top and bottom of the panel in order to make the pattern easier to see. Together, the profiles are consistent with a spiral pattern where the opacity maxima shift to smaller radii as the phase increases following the dotted lines (included to guide the eye), as expected for a trailing wave. Also, there does appear to be a single arm, as expected for an $|m| = 1$ pattern. However, the wavelength of the pattern clearly gets smaller with increasing radius, which implies that it is propagating outwards, which is inconsistent with its fast pattern speed.

Probably the simplest way to reconcile W85.67's morphology and pattern speed is for it to be a bending wave instead of a density wave. Bending waves propagate in the opposite direction from density waves, so an outward-propagating bending wave would be due to an outer vertical resonance, and thus have a higher pattern speed than the local mean motion, as we observe. However, there are major problems with identifying this feature as a bending wave. First, we do not observe the viewing-angle-dependent effects expected for bending waves. If the observed opacity variations were due to vertical structure, they should become more prominent at lower ring opening angles, and this is not observed. Also, the positions of maxima and minima should depend not only on the phase of the pattern but also the observation geometry, but if we include these effects in our analysis, it does not reduce the residuals from the best-fitting solution. In fact, with these corrections we found no useful minima for any value of m. Finally, the pattern speed of this wave is not appropriate for a bending wave. An $m = -1$ bending wave at this location would have a pattern speed of around $2362^\circ\ \mathrm{d}^{-1}$, which is very different from the observed value, and there is no strong minimum at that pattern speed. Together, these findings strongly suggest that this feature is not a bending wave.

Instead, the apparent incongruity between W85.67's morphology and pattern speed could be explained by another unusual feature of this wave: it appears to be drifting slowly through the ring. Fig. 18 shows representative profiles of this wave obtained by VIMS, along with the profile derived from the *Voyager* radio science experiment. These profiles clearly demonstrate that the wave has moved inwards between the *Voyager* epoch (when it was centred around 85 700 km) and the *Cassini* era (where it was closer to 85 680 km). Even within the span of *Cassini* observations, we can see that the wave has continued to move inwards, and is now approaching the inner edge of the plateau.

A slightly different way to visualize these changes is to plot the dominant pattern wavelength in the profile as a function of radius.

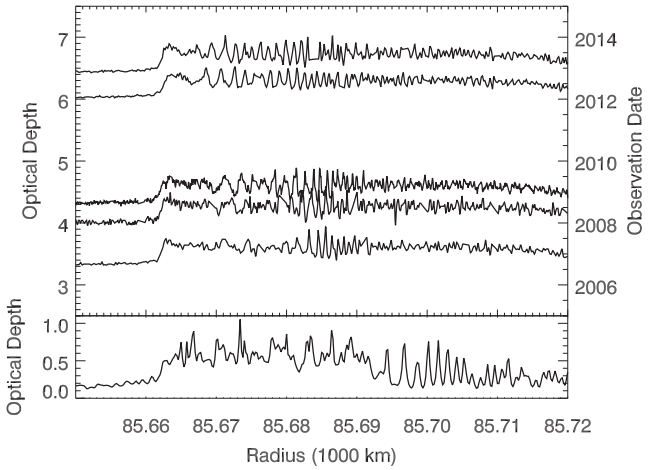

Figure 18. Profiles of W85.67 obtained over a broad range of times by *Cassini* and *Voyager*. The bottom panel shows the RSS profile of this wave obtained by *Voyager 1* in 1980. The top panel shows six profiles obtained by VIMS during the following occultations: Rev 41 α Aurigua, Rev 77 γ Crucis, Rev 106 R Cassiopea, Rev 170 β Pegasi, Rev 193 μ Cephii. These profiles have been vertically offset by amounts proportional to the time separation between them. We see clearly that the wave pattern has been moving inwards over time.

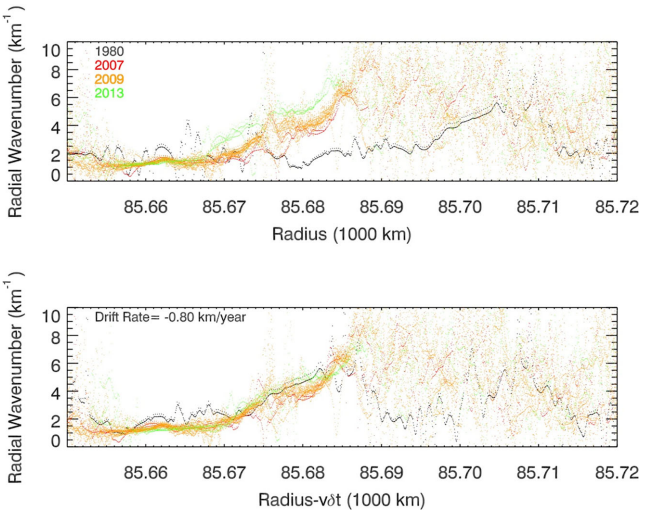

Figure 19. Plots showing the dominant radial wavenumber of the occultation profiles around W85.67, derived from wavelet analyses. The top panel shows wavenumber profiles derived from the *Voyager* RSS occultation in black and the *Cassini* VIMS occultations in various colours. Within the wave, the wavenumber increases linearly with radius, as expected, but the location of this ramp moves steadily inwards over time. The bottom panel shows the same profiles, shifted relative to each other assuming a constant drift rate of -0.8 km yr^{-1}. The wavenumber ramps all align in this case, indicating that the resonance has been moving inwards at approximately this rate for the last 30 yr.

As in our previous wavelet analysis, we use a wavelet transform and compute the power-weighted phase of the profile as a function of radius $\phi(r)$. The radial derivative of this phase parameter $\mathrm{d}\phi/\mathrm{d}r$ then provides an estimate of the dominant wavenumber in the profile as a function of radius. Fig. 19 shows the wavenumber profiles for the various *Cassini* and *Voyager* occultations. In each profile, the wave appears as a nearly linear ramp in wavenumber. If we assume the wave has been moving steadily inwards at a rate of

around 0.8 km yr^{-1}, then the *Voyager* and *Cassini* profiles can be aligned fairly well. It therefore appears that this wave has been moving inwards at around 0.8 km yr^{-1} for the last 30 yr. Given the wave could be moving through regions of different surface mass densities (which also influence the wavelengths), we cannot yet provide a more precise estimate of this rate or a robust estimate of the uncertainty on this parameter. However, even this rough estimate of the wave's motion has important implications for the wave's morphology because it is comparable to the wave's group velocity.

Waves in planetary rings have a finite group velocity, so these features cannot respond instantaneously to changes in the perturbing forces. The group velocity of a density wave in Saturn's rings is given by the following expression (Shu 1984):

$$|v_g| = \pi G \sigma_0 / \kappa, \tag{6}$$

where G is the universal gravitational constant, σ_0 is the ring's local surface density and κ is the local radial epicyclic frequency, which is about 0.00025 s^{-1} in this part of the C-ring. The group velocity in this region is therefore $0.26(\sigma_0/1\ \mathrm{g\ cm^{-2}})$ km yr^{-1}. This means that if the local surface mass density of this plateau is less than 3 g cm^{-2}, then the resonant radius is moving faster than the wave's group velocity. Given that the $m = 3$ waves in adjacent plateaux indicate mass densities of order a few grams per square centimetre (see Fig. 14), this condition could indeed be met.

If the resonant radius is indeed moving radially faster than the wave itself can propagate, then the morphology of the wave can be significantly distorted. The clearest illustration of this phenomenon comes from the waves generated by the co-orbital moons Janus and Epimetheus. These two moons swap orbital positions every 4 yr, and so the precise resonance locations move back and forth in the rings. As a result, the waves they generate exhibit a complex, time variable morphology. However, Tiscareno et al. (2006) showed that the morphology of these waves can be modelled as the superposition of multiple components, each propagating at a finite speed from a particular source location. Applying the same basic concept to W85.67 yields some useful insights into this wave's structure.

First consider a wave generated by a perturbation with a fixed period, so that the resonant location r_L is fixed. In this case, at any location r we are seeing a piece of the wave that was generated a time $\delta t = (r - r_L)/v_g$ before the wave was observed (note we take v_g to be negative for an inward propagating wave). But what if instead the resonance location is itself moving at a speed v_L? If we observe the wave at a radius r, then we must consider both the location of the resonance now r_{L0} and the location of the resonance when the wave now observed at r was first generated, which we will denote r_{L1}. Let us now say δt is the time it took the wave to move from r_{L1} to r, which is also the time it takes the resonance to move from r_{L1} to r_{L0}. Hence we have the two equations $\delta t = (r - r_{L1})/v_g$ and $\delta t = (r_{L0} - r_{L1})/v_L$. Combining these two expressions, we find $(r - r_{L1})/v_g = (r_{L0} - r_{L1})/v_L$, which allows us to relate the distance $r - r_{L1}$ to the distance from the current resonant location $r - r_{L0}$:

$$r - r_{L0} = r - r_{L1} + r_{L1} - r_{L0} = (1 - v_L/v_g)(r - r_{L1}).$$

Note that $r - r_{L1}$ corresponds to the distance between the observation point and the resonant radius when the resonant location is fixed. By contrast, $r - r_{L0}$ is the distance between the observed point and the current resonance position. Thus a wave with a moving resonance has its radial profile distorted by a factor of $1 - v_L/v_g$. Now, if this is really an $m = -1$ wave, it should be propagating inwards, so $v_g < 0$, but the wave also appears to be moving inwards, so $v_L < 0$ as well. If $|v_L| > |v_g|$, then $1 - v_L/v_g$ will be negative, and the wave will appear on the opposite side of the *current* resonance location from what one would expect for a wave with a fixed resonance frequency.

To clarify what the wave itself would look like in this situation, let us first consider a standard density wave with a fixed resonant radius. In this case, the phase of the wave is given by the following expression:

$$\phi_{tot} = \phi + \phi_r(r) = |m|(\lambda - \Omega_p t) + \int_{r_L}^{r} k(r')\mathrm{d}r', \tag{7}$$

where $k(r')$ is the radial wavenumber. For waves with $m \neq +1$, $k(r')$ is given by the following asymptotic expression:

$$k(r') \simeq \frac{3M_s}{2\pi\sigma_0 r_L^4}(m-1)(r' - r_L) = \chi(m-1)(r' - r_L), \tag{8}$$

where M_s is Saturn's mass and σ_0 is the undisturbed surface mass density of the ring.[9] If we now consider a wave produced by a moving resonance, we need to replace r_L in the above expressions with either r_{L0} or r_{L1}. As mentioned above, the wavenumber of a density wave is determined by how far the wave has propagated from its source region, so the factor of $(r' - r_L)$ in the above expression for $k(r')$ should be replaced with $(r' - r_{L1}) = (r' - r_{L0})/(1 - v_L/v_g)$, so in this case the expression for the wavenumber becomes

$$k(r') \simeq \chi(m-1)\frac{(r' - r_{L0})}{(1 - v_L/v_g)}. \tag{9}$$

Since k must be positive, this means that if $|v_L| > |v_g|$ the wave will appear on the opposite side of r_{L0} and the radial trends in the pattern's wavelength will be reversed, as we observe. On the other hand, when we integrate the wavenumber to obtain the phase, we should choose r_{L0} as the lower limit of integration, because we are considering the appearance of the wave at a single moment in time. Hence we expect that the appropriate generalization of equation (7) to be

$$\phi_{tot} = |m|(\lambda - \Omega_p t) + \frac{\chi}{2}(m-1)\frac{(r - r_{L0})^2}{(1 - v_L/v_g)}. \tag{10}$$

If we observe the ring at one time, then a line of constant phase is described by the following equation:

$$\frac{\mathrm{d}\lambda}{\mathrm{d}r} = -\frac{\chi(m-1)}{|m|}\frac{(r - r_{L0})}{(1 - v_L/v_g)}. \tag{11}$$

Note that if $|v_L| > |v_g|$, both $1 - v_L/v_g$ and $r - r_{L0}$ change sign, which leaves the slope of this curve unchanged. Hence the wave remains a trailing spiral regardless of whether $|v_L| > |v_g|$ or not, which is consistent with our observations (see Fig. 17).

We can therefore accommodate the pattern speed and the morphology of the wave so long as the resonance moves through the ring faster than the group velocity, which effectively turns the wave 'inside-out'. Furthermore, this slow drift in the resonant radius induces slight phase shifts that slightly modify the wave's apparent pattern speed. This probably explains why the best-fitting pattern

[9] Note that k is positive exterior to the resonance for $m > 0$ (inner Lindblad resonances) and interior to the resonance for $m < 0$ (outer Lindblad resonances).

speed in Fig. 16 is slightly slower than expected and the phase difference residuals have a rather large scatter.

At present, we have no clear explanation for why the resonant radius would be migrating in the first place, but we strongly suspect this feature is driven by some structure inside Saturn. Note the pattern speed of this structure is 2430 d^{-1}, which is roughly three times Saturn's rotation period. Since the pattern speed is much faster than the planet's internal rotation rate, this structure cannot be a persistent anomaly carried around by Saturn's winds. It might represent some sort of normal model oscillation, but sectoral ($\ell = m$) modes with $m = 1$ are forbidden (because they would entail a displacement of the planet's centre of mass). Modes such as $[\ell = 3, m = 1]$ are possible and could potentially drive $m = -1$ waves in the rings, but these resonances were not predicted to occur at W85.67's location (Marley & Porco 1993; Marley 2014). Another intriguing coincidence is that in a reference frame rotating with Saturn, this pattern would be moving prograde at roughly twice the planet's rotation rate. This is the maximum rotation rate allowed for inertial waves inside a fluid planet (Wu 2005). Even though inertial waves do not generate strong gravitational perturbations, this coincidence might suggest some connection with those sorts of oscillations (we thank J. Fuller for pointing this out). In any case, the steady change in the oscillation frequency would imply secular evolution of something in Saturn's interior.

8 SUMMARY

Table 5 provides the m-numbers and pattern speeds of all the previously unidentified waves securely identified by Hedman & Nicholson (2013) and this work, along with the corresponding estimates of the ring's surface mass density and opacity for those features (based on fits by Baillié et al. 2011). We may summarize the results of this analysis as follows.

(i) Wave W83.63 appears to be an $m = -10$ wave, which could be generated by a resonance with an $m = 10$ fundamental sectoral normal mode in the planet.

(ii) If W83.63 is generated by an $m = 10$ planetary normal mode, then that mode must have a larger amplitude than the modes with $m = 5$–9, which do not appear to generate waves of comparable strength.

(iii) The identification of wave W81.02 is still uncertain. It could be $m = -11$ or -5. The former result seems more consistent with the observations, but the wave's location could favour the latter option.

(iv) There are no less than five $m = +3$ waves with pattern speeds between 807 and 834° d^{-1}. Since these pattern speeds are close to the planet's rotation rate, they are probably driven by 3:2 tesseral resonances with persistent gravitational anomalies in the planet.

(v) The surface mass densities of the plateaux derived from the $m = +3$ waves are comparable to or less than the surface mass densities of the background ring derived from inward-propagating waves. The optical depth enhancement in the plateaux therefore must be due to a change in the internal mass densities or size distribution of the ring particles, rather than to the amount of ring material per unit area.

(vi) The W85.67 wave appears to be an $m = -1$ pattern that is drifting inwards through the rings at a rate of about 0.8 km yr^{-1}. The high pattern speed of this structure suggests it is generated by a resonance with some dynamic structure inside Saturn, but it remains unclear what sort of planetary perturbation produces this feature, or why the resonance location is moving.

ACKNOWLEDGEMENTS

We wish to thank NASA, the *Cassini* project and especially the VIMS team for providing the data used in this analysis. We also thank R. G. French for providing refined geometry information for the occultation data. We had useful conservations with K. Baillié and J. Fuller, and M. Marley provided helpful comments on the first draft of this paper.

REFERENCES

Anderson J. D., Schubert G., 2007, Science, 317, 1384
Andrews D. J., Cowley S. W. H., Dougherty M. K., Lamy L., Provan G., Southwood D. J., 2012, J. Geophys. Res. (Space Phys.), 117, 4224
Baillié K., Colwell J. E., Lissauer J. J., Esposito L. W., Sremčević M., 2011, Icarus, 216, 292
Brown R. H. et al., 2004, Space Sci. Rev., 115, 111
Colwell J. E., Nicholson P. D., Tiscareno M. S., Murray C. D., French R. G., Marouf E. A., 2009, in Dougherty M. K., Esposito L. W., Krimigis S. M., eds, Saturn from Cassini-Huygens. Springer-Verlag, Berlin, p. 375
Colwell J. E., Cooney J. H., Esposito L. W., 2011, in EPSC-DPS Joint Meeting 2011, Particle Size Variations in Saturn's Rings from Occultation Statistics. p. 1282
Cowley S. W. H., Provan G., 2013, J. Geophys. Res. (Space Phys.), 118, 7246
Cuzzi J., Clark R., Filacchione G., French R., Johnson R., Marouf E., Spilker L., 2009, in Dougherty M. K., Esposito L. W., Krimigis S. M., eds, Saturn from Cassini-Huygens. Springer-Verlag, Berlin, p. 459
Davies M. E., Abalakin V. K., Lieske J. H., Seidelmann P. K., Sinclair A. T., Sinzi A. M., Smith B. A., Tjuflin Y. S., 1983, Celest. Mech., 29, 309
Dyudina U. A. et al., 2007, Icarus, 190, 545
Franklin F. A., Colombo G., Cook A. F., 1982, Nature, 295, 128
Fuller J., Lai D., Storch N. I., 2014, Icarus, 231, 34
García-Melendo E., Pérez-Hoyos S., Sánchez-Lavega A., Hueso R., 2011, Icarus, 215, 62
Goldreich P., Kumar P., 1988, ApJ, 326, 462
Goldreich P., Kumar P., 1990, ApJ, 363, 694
Hedman M. M., Nicholson P. D., 2013, AJ, 146, 12
Hedman M. M., Burns J. A., Tiscareno M. S., Porco C. C., 2009, Icarus, 202, 260
Holberg J. B., Forrester W. T., Lissauer J. J., 1982, Nature, 297, 115
Lamy L., 2011, in Planetary, Solar and Heliospheric Radio Emissions (PRE VII). p. 38, preprint (arXiv:1102.3099)
Marley M. S., 1990, PhD thesis, Arizona Univ., Tucson
Marley M. S., 1991, Icarus, 94, 420
Marley M. S., 2014, Icarus, 234, 194
Marley M. S., Porco C. C., 1993, Icarus, 106, 508
Mitchell C. J., Porco C. C., Dones H. L., Spitale J. N., 2013, Icarus, 225, 446
Perryman M. A. C. et al., 1997, A&A, 323, L49
Porco C. C., 1983, PhD thesis, California Institute of Technology, Pasadena
Porco C. C., Danielson G. E., 1982, AJ, 87, 826
Provan G., Cowley S. W. H., Sandhu J., Andrews D. J., Dougherty M. K., 2013, J. Geophys. Res. (Space Phys.), 118, 3243
Read P. L., Dowling T. E., Schubert G., 2009, Nature, 460, 608
Rosen P. A., Tyler G. L., Marouf E. A., Lissauer J. J., 1991, Icarus, 93, 25
Sánchez-Lavega A. et al., 2014, Geophys. Res. Lett., 41, 1425
Sayanagi K. M. et al., 2013, Icarus, 223, 460
Sayanagi K. M., Dyudina U. A., Ewald S. P., Muro G. D., Ingersoll A. P., 2014, Icarus, 229, 170
Shu F. H., 1984, in Greenberg R., Brahic A., eds, Planetary Rings. Univ. Arizona Press, Tucson, p. 513
Tiscareno M. S., Nicholson P. D., Burns J. A., Hedman M. M., Porco C. C., 2006, ApJ, 651, L65

Torrence C., Compo G. P., 1998, Bull. Am. Meteorol. Soc., 79, 61
Wu Y., 2005, ApJ, 635, 674
Ye S.-Y., Gurnett D. A., Groene J. B., Wang Z., Kurth W. S., 2010, J. Geophys. Res. (Space Phys.), 115, 12258

SUPPORTING INFORMATION

Additional Supporting Information may be found in the online version of this article:

Table 4. Time, longitude and phase differences used to determine pattern speeds.

(http://mnras.oxfordjournals.org/lookup/suppl/doi:10.1093/mnras/stu1503/-/DC1).

Please note: Oxford University Press are not responsible for the content or functionality of any supporting materials supplied by the authors. Any queries (other than missing material) should be directed to the corresponding author for the article.

This paper has been typeset from a TEX/LATEX file prepared by the author.